MOX-Report No. 24/2018

Direct and Large Eddy Simulation of three-dimensional non-Boussinesq gravity currents with a high order DG method

Bassi, C.; Abbà, A.; Bonaventura,L.; Valdettaro,L.

Direct and Large Eddy Simulation of three-dimensional non-Boussinesq gravity currents with a high order DG method

Caterina Bassi[1]

Antonella Abbà [2], Luca Bonaventura [1], Lorenzo Valdettaro [1]

April 11, 2018

[1] MOX – Modelling and Scientific Computing,
Dipartimento di Matematica, Politecnico di Milano
Via Bonardi 9, 20133 Milano, Italy
caterina.bassi@polimi.it, luca.bonaventura@polimi.it,
lorenzo.valdettaro@polimi.it
[2] Dipartimento di Scienze e Tecnologia Aerospaziali, Politecnico di Milano
Via La Masa 34, 20156 Milano, Italy
antonella.abba@polimi.it

1

Abstract

We present results of three-dimensional Direct Numerical Simulations (DNS) and Large Eddy Simulations (LES) of turbulent gravity currents with a Discontinuous Galerkin (DG) Finite Elements method. In particular, we consider the three-dimensional lock-exchange test case as a typical benchmark for gravity currents. Since, to the best of our knowledge, non-Boussinesq three-dimensional reference DNS are not available in the literature for this test case, we first perform a DNS experiment. The three-dimensional DNS allows to correctly capture the loss of coherence of the three-dimensional turbulent structures, providing an accurate description of the turbulent phenomena taking place in gravity currents. The three-dimensional DNS is then employed to assess the performance of different LES models. In particular, we have considered the Smagorinsky model, the isotropic dynamic model and an anisotropic dynamic model. The LES results highlight the excessively dissipative nature of the Smagorinsky model with respect to the dynamic models and the fact that the anisotropic dynamic model performs slightly better with respect to its isotropic counterpart.

2

1 Introduction

Gravity currents, arising when a heavier fluid propagates into a lighter one in a predominantly horizontal direction, are very common in geophysical flows. In atmospheric gravity currents the density difference is typically caused by the temperature difference between the cold front and the warmer surrounding air. In oceanic flows, density differences are caused instead by salinity and temperature gradients, while in pyroclastic flows the density difference is due to the presence of suspended particles in the flow. A comprehensive description of environmental gravity currents can be found e.g. in [33]. In gravity currents, the density difference between the lighter and heavier fluid can range from very small to very large. In case of small density differences, density variations in the momentum equation can be neglected in the inertia term, but retained in the buoyancy term, yielding the so called Boussinesq approximation, see e.g. [20]. This approximation has been employed in most experimental and computational studies of gravity currents reported in the literature, see e.g. [24], [29], [30]. However, in several of the above listed phenomena, non-Boussinesq effects become important.

Gravity currents appear to be a particularly interesting phenomenon from the point of view of turbulence modelling, since a wide range of interesting phenomena arise, such as breaking internal waves and Kelvin-Helmholtz instabilities. Moreover, in gravity currents, especially in the non-Boussinesq regime, consistent density differences are present. As a consequence, gravity currents can also be a good candidate for the validation of turbulence models for compressible flows with major density differences.

The main purpose of the present work is to present the first DNS results for a gravity current benchmark in the non-Boussinesq regime. More specifically, a three-dimensional lock exchange problem analogous to that studied in [29] was simulated. With respect to the two-dimensional DNS already present in the literature, see e.g. [6], the three-dimensional DNS allows to effectively capture the vortex stretching and the loss of coherence of the three-dimensional coherent structures, providing more insight in the turbulent phenomena arising in gravity currents. The DNS results have then been employed for the assessment of different subgrid LES models, including more conventional ones, such as the Smagorinsky model [34] and the isotropic dynamic model [19], and less conventional ones, such as an anisotropic dynamic model [2].

The numerical framework chosen to implement the models is that of a Discontinuous Galerkin discretization. Such a framework

allows to generalize the concept of LES filter as a projection onto the polynomial space related to the discretization, thus making it possible to apply it to arbitrary unstructured meshes. This is conceptually similar to what is done in Variational Multi-Scale (VMS) models, see e.g. [25], [27].

The LES results confirm the excessively dissipative nature of the Smagorinsky model with respect to the dynamic models and the fact that the anisotropic dynamic model performs slightly better with respect to its isotropic counterpart. As a result, we also extend to the variable density case and to a three-dimensional configuration the findings in [1], [9] on the importance of more complex dynamical models for subgrid modeling also in the VMS framework.

The paper is organized as follows. Section 2 provides a brief introduction of the mathematical model employed for the treatment of turbulent gravity currents, while for a more detailed description of the different subgrid turbulence models and of the Discontinuous Galerkin method we refer to the appendix A and B, respectively. The set-up of the DNS and LES experiments is described in section 3. The DNS results are discussed in section 4, while the LES are presented in section 5 and their quality assessed in terms of the corresponding DNS. Some conclusions and perspectives for future work are presented in section 6.

2   The mathematical model

We provide in this section a short overview the mathematical model we employ for the description of gravity currents. The model is based on the Navier-Stokes equations, filtered with the same procedure as in [1], [9]. The filtering operator, which is denoted by $\overline{\cdot}$, is in-built in the DG discretization approach and is described in detail in appendix B. Here, we only point out that the filter $\overline{\cdot}$ is defined as the projection onto a space of piecewise polynomial functions of degree p, where p denotes the degree of the piecewise polynomial basis functions employed by the DG method. The choice of p implicitly defines a spatial filter scale Δ, whose full definition is given in appendix B.

The Favre filter operator $\widetilde{\cdot}$ (see e.g. [16]) is then defined implicitly by the Favre decomposition, which is given for a generic function f by

$$\overline{\rho f} = \overline{\rho}\widetilde{f}. \tag{1}$$

4

The filtered Navier-Stokes equations we employ can be written as:

$$\partial_t \overline{\rho} + \partial_j (\overline{\rho} \widetilde{u}_j) = 0 \tag{2a}$$

$$\partial_t (\overline{\rho} \widetilde{u}_i) + \partial_j (\overline{\rho} \widetilde{u}_i \widetilde{u}_j) + \partial_i \overline{p} - \partial_j \widetilde{\sigma}_{ij}$$
$$= -\partial_j \tau_{ij} + \overline{\rho} f_i \tag{2b}$$

$$\partial_t (\overline{\rho} \widetilde{e}) + \partial_j \left(\overline{\rho} \widetilde{h} \widetilde{u}_j \right) - \partial_j (\widetilde{u}_i \widetilde{\sigma}_{ij}) + \partial_j \widetilde{q}_j \tag{2c}$$
$$= -\frac{1}{(\gamma - 1)Ma^2} \partial_j Q_j^{\text{sgs}} - \frac{1}{2} \partial_j \left(J_j^{\text{sgs}} - \tau_{kk} \widetilde{u}_j \right) + \overline{\rho} f_j \widetilde{u}_j.$$

Here, $\widetilde{\sigma}_{ij}$ and $\widetilde{q}_i$ are the filtered diffusive fluxes, for which the following expressions are assumed:

$$\widetilde{\sigma}_{ij} = \mu \widetilde{\mathcal{S}}_{ij}^d, \qquad \widetilde{q}_i = -\lambda \partial_i \widetilde{T}, \tag{3}$$

with $\widetilde{\mathcal{S}}_{ij} = \partial_j \widetilde{u}_i + \partial_i \widetilde{u}_j$ and $\widetilde{\mathcal{S}}_{ij}^d = \widetilde{\mathcal{S}}_{ij} - \frac{1}{3} \widetilde{\mathcal{S}}_{kk} \delta_{ij}$. τ_{ij}, Q_j^{sgs} and J_j^{sgs} are the subgrid stress tensor, the subgrid temperature flux and the subgrid turbulent diffusion flux, respectively, whose expressions are:

$$\tau_{ij} = \overline{\rho u_i u_j} - \overline{\rho} \widetilde{u}_i \widetilde{u}_j, \tag{4a}$$

$$Q_i^{\text{sgs}} = \overline{\rho u_i T} - \overline{\rho} \widetilde{u}_i \widetilde{T} = \overline{\rho} \left(\widetilde{u_i T} - \widetilde{u}_i \widetilde{T} \right), \tag{4b}$$

$$J_i^{\text{sgs}} = \overline{\rho u_i u_k u_k} - \overline{\rho} \widetilde{u}_i \widetilde{u}_k \widetilde{u}_k = \overline{\rho \widetilde{u_i u_k u_k}} - \overline{\rho} \widetilde{u}_i \widetilde{u}_k \widetilde{u}_k$$
$$= \tau(u_i, u_k, u_k) + 2 \widetilde{u}_k \tau_{ik} + \widetilde{u}_i \tau_{kk}. \tag{4c}$$

In the last equality of equation (4c), the generalized central moments $\tau(u_i, u_j, u_k) = \overline{\rho \widetilde{u_i u_j u_k}} - \widetilde{u}_i \tau_{jk} - \widetilde{u}_j \tau_{ik} - \widetilde{u}_k \tau_{ij} - \overline{\rho} \widetilde{u}_i \widetilde{u}_j \widetilde{u}_k$ (see [17]) have been introduced.

These subgrid terms just introduced need modeling. In this work, we have employed the Smagorinsky model [34], the isotropic dynamic model [19] and the anisotropic dynamic model proposed in [2]. A complete description of the subgrid models is given in appendix A.

3 Set-up of the numerical experiments and definition of diagnostic quantities

We have carried out the DNS and the LES of a three-dimensional lock exchange problem at two different Reynolds numbers ($Re = 3000$ and $Re = 6000$), following the experimental setting of [29] for the definition of the domain and the initial and boundary conditions. Notice that, however, we have considered a density ratio $\gamma_r = 0.7$,
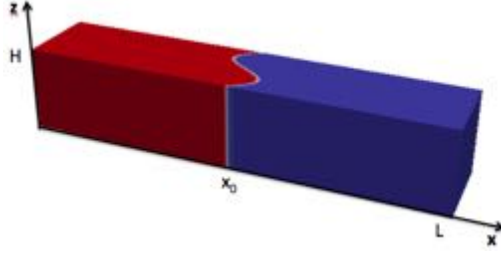
Figure 1: Initial density datum for the lock-exchange test case.

thus working in a non-Boussinesq regime, contrary to what was done in [29], where simulations in the Boussinesq regime were carried out.

The initial condition is presented in figure 1. The domain length is $L = 5$, its height is $H = 1$, its width is $W = 1$, while the position of the initial discontinuity is $x_0 = 2.5$. The initial density datum is characterized by a sharp transition layer. Moreover, a perturbation is applied in the spanwise direction in order to ease the transition to turbulence, so that

$$\rho_0(x, y, z) = \begin{cases} 1 & \text{if } 0 \leq x < a \\ 1 + 100(\gamma_r - 1)(x/L + 0.495 - \eta) & \text{if } a \leq x < b \\ \gamma_r & \text{if } b \leq x \leq L, \end{cases}$$

where $a = L/2 - (0.005 + \eta)L$, $b = L/2 + (0.005 - \eta)L$, $\eta = 0.05 \sin(2\pi \frac{y}{W})$ and W is the width of the domain.

The initial pressure at the top of the domain is defined as in [9]:

$$p_{init}^{top} = \frac{1}{\gamma Ma^2}, \tag{5}$$

where γ is the ratio between the specific heats and $Ma = 0.1$. An hydrostatic pressure profile is assumed in the rest of the domain. The initial temperature profile is computed from density and pressure using the equation of state for ideal gases. According to the non-dimensionalization employed in the present work (which is the same as in [9] and [8]), the Froude number can be expressed as:

$$Fr = \sqrt{1 - \gamma_r}, \tag{6}$$

where γ_r is the ratio between the densities on the left and on the right with respect to the initial discontinuity.

We employ slip boundary conditions in the streamwise and vertical directions, while periodic boundary conditions are imposed in the spanwise direction.

6

For the time discretization, a fourth order accurate, Strong Stability Preserving explicit Runge-Kutta method, see e.g. [35], has been employed for all the simulations.

In order to analyze quantitatively the DNS results and to assess the ability of the different LES models in reproducing them, various diagnostic quantities have been considered. The temporal evolution of the dissipated energy was computed integrating in time the following equation:

$$\frac{dE_d}{dt} = \int_{\Omega} \left\{ \rho\nu \left[\frac{1}{2}(\partial_j u_i + \partial_i u_j)^2 - \frac{2}{3}(\nabla \cdot \mathbf{u})^2 \right] \right\} d\mathbf{x}. \qquad (7)$$

It should be noticed that the contribution of the subgrid scale viscosity ν_{sgs} is added to the molecular viscosity ν in the previous equation when an LES realized with the Smagorinsky model or with the isotropic dynamic model is considered. Since, for the anisotropic dynamic model, the isotropic and deviatoric parts of the subgrid-scale stress in the momentum equation are modeled together, the temporal evolution of the dissipated energy was computed integrating the following equation:

$$\frac{dE_d}{dt} = \int_{\Omega} \left\{ \rho\nu \left[\frac{1}{2}(\partial_j u_i + \partial_i u_j)^2 - \frac{2}{3}(\nabla \cdot \mathbf{u})^2 \right] - \partial_i u_j \tau_{ij}^d \right\} d\mathbf{x}, \quad (8)$$

where τ_{ij}^d is the deviatoric part of the subgrid scale stress tensor.

The second diagnostic quantity we have considered is the time evolution of the Reference Potential Energy (RPE). This quantity, which has been first introduced in [42], corresponds to the minimum potential energy that can be obtained through an adiabatic redistribution of the fluid. Starting from the potential energy E_p and the reference potential energy RPE, we can compute the available potential energy (APE) as:

$$APE(t) = E_p(t) - RPE(t). \qquad (9)$$

As discussed in [42], the APE is the part of the potential energy that can actually be transferred to kinetic energy because of the turbulent mixing.

As pointed out in [42] and recalled in [29], the reference potential energy increases with time, thanks to the stratified mixing: the RPE is, as a consequence, an effective measure of how much mixing has occurred in the fluid. We have computed the RPE following the procedure outlined in [37]. We have introduced the density variable $\tilde{\rho}$ in the sample space $[\rho_m, \rho_M]$, with ρ_m and ρ_M minimum and maximum densities, respectively. The probability of density ρ to

be in the interval $[\tilde{\rho}, \tilde{\rho} + d\tilde{\rho}]$ is denoted by $P(\tilde{\rho})d\tilde{\rho}$, where $P(\tilde{\rho})$ is a probability density function. This function is estimated in practice dividing the density interval $[\rho_m, \rho_M]$ into different bins. The density field is then scanned and, for each element, we consider the density value in each Gauss integration point. If the value falls into a particular bin, a quantity equal to the Gauss weight associated to the Gauss point is accounted for that bin. The probability density function is then obtained normalizing the volume contained in each bin by the volume of the whole domain, after the completion of the whole scanning procedure.

The quantity $Z_r(\rho)$ is the height of the fluid of density ρ in the minimum potential energy state, while dZ_r is the thickness of the layer containing fluid of density between $\tilde{\rho}$ and $\tilde{\rho} + d\tilde{\rho}$. If the layers have the same horizontal surface A, the volume occupied by this layer of fluid is:

$$AdZ_r|_\rho = |\Omega|P(\tilde{\rho})d\tilde{\rho}|_\rho.$$

This equation is then integrated over $\tilde{\rho}$ in order to obtain the profile $Z_r(\rho)$:

$$Z_r(\rho) = H \int_\rho^{\rho_M} P(\tilde{\rho})d\tilde{\rho}. \tag{10}$$

Since the RPE is defined as the potential energy of the reference state, whose vertical profile is given by equation (10), the following equation was employed for its computation:

$$RPE = \frac{1}{Fr^2}LW \int_0^H \rho(Z_r)Z_r dZ_r, \tag{11}$$

where $\rho(Z_r)$ is the reference density expressed as a function of the reference coordinate Z_r.

We have also compared the results of the different simulations in terms of instantaneous fields at different instants of time. We have considered in particular density fields and $Q-$criterion fields. This criterion has been introduced in [26] by identifying a vortex as a spatial region where the Euclidean norm of the vorticity tensor dominates that of the strain rate, i.e.:

$$Q = \frac{1}{2}\left(\frac{1}{4}|\Omega|^2 - \frac{1}{4}|\mathcal{S}^d|^2\right) > 0, \tag{12}$$

where $\mathcal{S}_{ij}^d = \partial_j u_i + \partial_i u_j - \frac{1}{3}(2\partial_k u_k)\delta_{ij}$ and $\Omega_{ij} = \partial_j u_i - \partial_i u_j$. Notice that the $Q-$criterion allows to distinguish between pure shearing motion and the actual swirling motion of a vortex.

$Re = 3000$	$Re = 6000$
3800000	3800000

Table 1: Number of DOFs associated to the DNS.

4 Results of the DNS experiments

In this section, the main results obtained from the DNS experiments are presented, to be compared in the following section with the corresponding LES results.

Concerning the spatial discretization, we have used as basis functions piecewise polynomials of degree $p = 4$. Notice that overintegration has been necessary in order to obtain stable simulations. Indeed, a number of integration points corresponding to exact integration of polynomials of degree 12 has been employed.

In table 1 the total number of degrees of freedom associated to the DNS is presented. The total number of DOFs employed for the DNS at Reynolds $Re = 3000$ is of the same order of magnitude as the one employed in [29] for the $med - res1$ simulation, realized with approximately 5000000 DOFs. In [29], two more resolved simulations, denoted by $med - res2$ and $high - res$, respectively, were also realized, but the authors stressed that the results of the three simulations were quite similar to each other. As a consequence we have decided to perform a simulation with a spatial resolution comparable to the $med - res1$ simulation. The total number of degrees of freedom for the DNS at Reynolds $Re = 6000$ is the same as the one for the DNS at $Re = 3000$: this implies that for $Re = 6000$ we have an underresolved DNS.

The computational grid for our computations was built starting from a structured hexahedral mesh. Each hexahedron is divided into N_t tetrahedra. The expressions for the equivalent grid spacings are:

$$\Delta_x = \frac{L}{N_x \sqrt[3]{N_t N_p}}, \quad \Delta_y = \frac{W}{N_y \sqrt[3]{N_t N_p}}, \quad \Delta_z = \frac{H}{N_z \sqrt[3]{N_t N_p}}, \quad (13)$$

where L, W and H are the length, width and height of the computational domain, respectively, N_x, N_y and N_z are the number of hexahedra in the x, y and z directions and N_p is the number of degrees of freedom per element when the polynomial degree is equal to p. In table 2 we present the values of N_x, N_y and N_z for the DNS. Following equations (13), the resolutions employed in the different directions for the DNS at $Re = 3000$ and for the under-resolved

DNS at Reynolds $Re = 6000$ are given by:

$$\Delta_x^{DNS} = 0.006, \quad \Delta_y^{DNS} = 0.004, \quad \Delta_z^{DNS} = 0.004. \qquad (14)$$

In order to verify if the DNS we are performing are well resolved, we compare these equivalent grid spacings to the non-dimensional Kolmogorov length scale. The dimensional form of the Kolmogorov length scale can be estimated as follows:

$$\eta^* = \left(\frac{\nu^{*3}}{\epsilon^*}\right)^{\frac{1}{4}}, \qquad (15)$$

where ν^* is the dimensional kinematic viscosity and ϵ^* is the dimensional kinetic energy dissipation. Notice that the symbol * identifies dimensional quantities. Following [29], we define the kinetic energy dissipation as:

$$\epsilon^* = \frac{cu_0^{*3}}{H^*}, \qquad (16)$$

where c is a constant which, in most cases, assumes values in the interval $[0.6, 0.8]$, u_0^* is a characteristic velocity and H^* is a characteristic length, which in our case corresponds to the height of the computational domain. In [29], the characteristic velocity is set equal to the velocity of the gravity current head as:

$$u_0^* = \frac{1}{2}\sqrt{\frac{g^*(\rho_1^* - \rho_2^*)H^*}{\rho_2^*}}, \qquad (17)$$

where ρ_1^* and ρ_2^*, with $\rho_1^* > \rho_2^*$, are the dimensional densities on the left and on the right of the initial discontinuity. The non-dimensionalization is carried out in the present work using the buoyancy velocity u_b^* defined as:

$$u_b^* = \sqrt{\frac{g^*(\rho_1^* - \rho_2^*)H^*}{\rho_1^*}}. \qquad (18)$$

As a consequence, u_0^* can be rewritten as:

$$u_0^* = \frac{1}{2}\sqrt{\frac{\rho_1^*}{\rho_2^*}}u_b^* = \frac{1}{2}\sqrt{\frac{\rho_1}{\rho_2}}u_b^*. \qquad (19)$$

We now rewrite equation (15) employing equations (16) and (19) and highlighting the non-dimensional quantities:

$$\eta H^* = \left(\frac{(\nu H^* u_b^*)^3}{\frac{c}{H^*}u_0^{*3}}\right)^{\frac{1}{4}} = \left(\frac{(\nu H^* u_b^*)^3}{\frac{c}{H^*}\left(\frac{1}{2}\sqrt{\frac{\rho_1}{\rho_2}}u_b^*\right)^3}\right)^{\frac{1}{4}}. \qquad (20)$$

10

$Re = 3000$	$Re = 6000$
$N_x = 56,\ N_y = 18,\ N_z = 18$	$N_x = 56,\ N_y = 18,\ N_z = 18$

Table 2: Number of hexahedra in the x, y, z directions associated to the DNS.

Simplifying, we get for the non-dimensional Kolmogorov length scale:

$$\eta = \left(\frac{\nu^3}{\frac{c}{8(\sqrt{\gamma_r})^3}} \right)^{\frac{1}{4}}, \tag{21}$$

where, as before, $\gamma_r = \rho_2/\rho_1$. For the kinematic viscosity, Sutherland's law is employed, obtaining:

$$\nu = \frac{T^\alpha}{\rho Re}. \tag{22}$$

As a result we obtain the following values:

$$\eta_{3000} = 0.004, \quad \eta_{6000} = 0.002. \tag{23}$$

If we compare the employed resolutions of equation (13) with the non-dimensional Kolmogorov length scales of the previous equation, we can claim that the DNS at $Re = 3000$ is quite well resolved, while the simulation at $Re = 6000$ is under-resolved. While we plan repeating the DNS at $Re = 6000$ at higher resolution as soon as computational resources are available, in this work we will employ it as a reference for the assessment of the different LES models, since the number of DOFs involved in these simulations is $N_{dofs} = 300000$, thus one order of magnitude smaller with respect to that of the under-resolved DNS (compare tables 1 and 3).

In figures 2(a) and 2(b) we show the density isosurfaces and the $Q = 5$ isosurface for the $Re = 3000$ DNS at $t = 9$. We can see that, for this lower Reynolds number, the flow field appears quite ordered with the presence of few turbulent structures.

In figures 3(a) and 3(b) we have instead the density isosurfaces and the $Q = 20$ isosurface for the $Re = 6000$ DNS at $t = 4$. The appearance of the vortices in figure 3(b) highlights, in this early phase of the simulation, a quite regular flow with relatively few turbulent structures even though, together with the Kelvin-Helmoltz spanwise rollers, also some longitudinal and horseshoe structures begin to appear.

In figures 4(a) and 4(b) we then consider the instantaneous density and Q profiles for the $Re = 6000$ DNS at a more advanced instant of time, $t = 9$. In particular if we look at figure 4(b), we
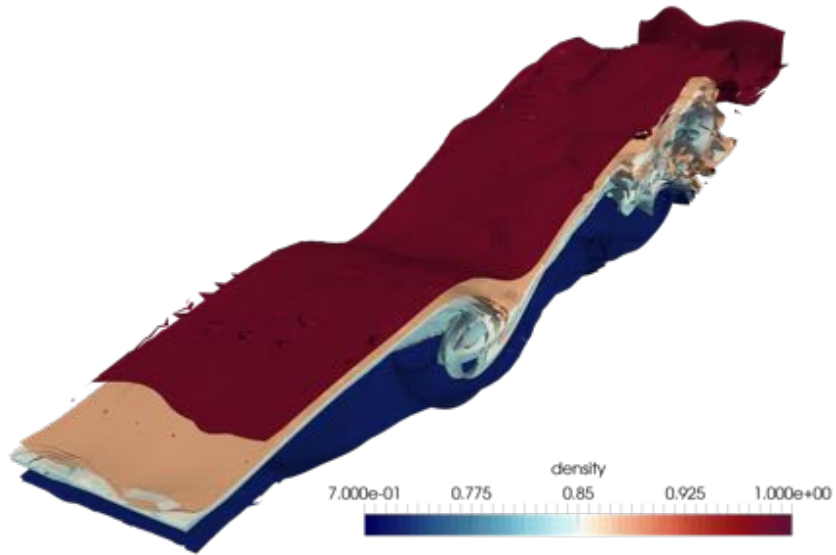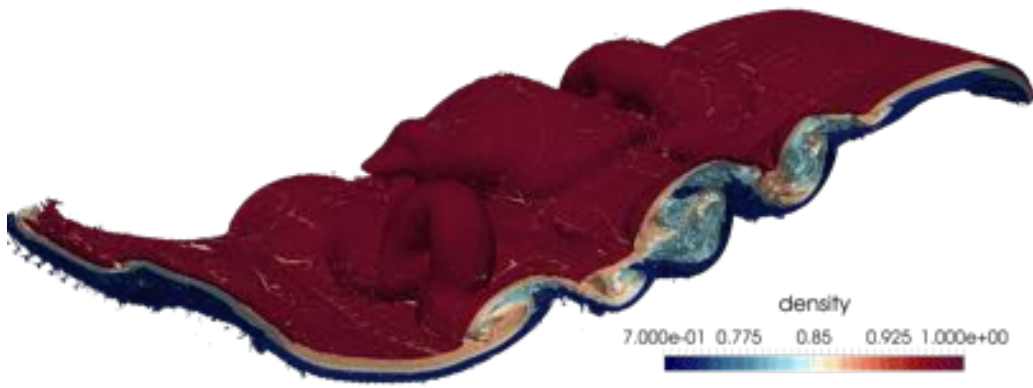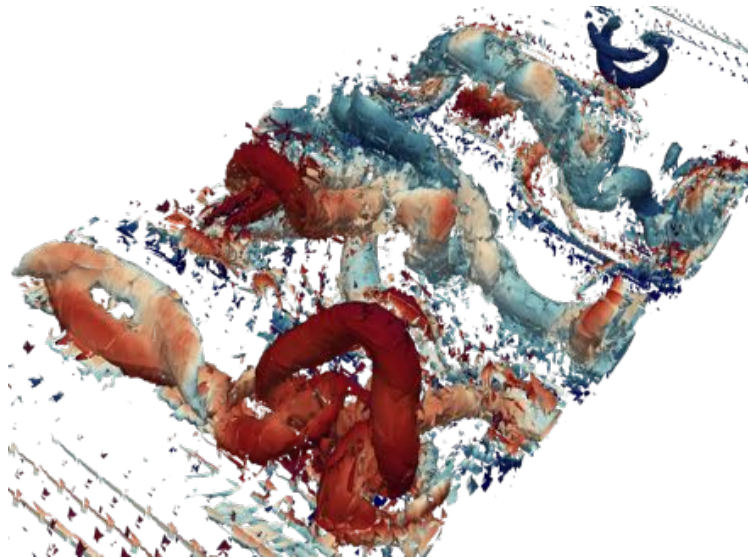
(a)
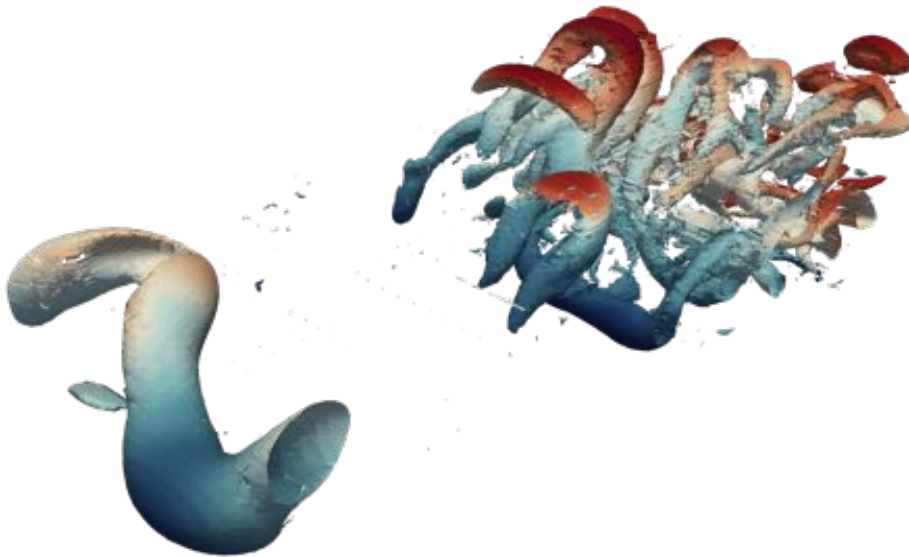
(b)

Figure 2: Isosurfaces at $t = 9$ for $Re = 3000$ (DNS) (a) density isosurfaces ($\rho = 0.72, 0.82, 0.85, 0.88, 0.98$). (b) $Q = 5$ isosurface (colored by density).

(a)

(b)

Figure 3: Isosurfaces at $t = 4$ for $Re = 6000$ (DNS) (a) density isosurfaces ($\rho = 0.72, 0.82, 0.85, 0.88, 0.98$). (b) $Q = 20$ isosurface (colored by density).

$Re = 3000$	$Re = 6000$
80000	300000

Table 3: Number of DOFs associated to the LES.

$Re = 3000$	$Re = 6000$
$N_x = 15,\ N_y = 5,\ N_z = 5$	$N_x = 23,\ N_y = 8,\ N_z = 8$

Table 4: Number of hexahedra in the x, y, z directions associated to the LES

can notice that the number of turbulent structures has considerably increased and that the flow is much more irregular with respect to the previous considered instant of time $t = 4$.

5   Results of the LES experiments

In this section, the main results obtained from the LES experiments are presented and assessed in comparison to the corresponding DNS.

Concerning the spatial discretization, as for the DNS, piecewise polynomials of degree $p = 4$ have been employed, while the polynomial degree associated to the test filter operation, neded to the dynamic models, was taken to be $\widehat{p} = 2$. Also in the LES case over-integration has been necessary in order to obtain stable simulations.

In table 3 the number of degrees of freedom associated to the different LES is presented. The number of degrees of freedom of the LES at $Re = 3000$ is of the same order of magnitude as the one employed in [29] for LES at the same Reynolds number. Following [32], the number of DOFs for the LES at $Re = 6000$ was obtained from the number of DOFs associated to the $Re = 3000$ LES as

$$N_{dofs}^{6000} = 2^{\frac{9}{4}} N_{dofs}^{3000}.$$

As for the DNS, the computational grid was built starting from a structured hexahedral mesh. The number of hexahedra in each spatial direction, N_x, N_y and N_z, is presented in table 4.

In table 5 we report the computational cost for the different simulations in terms of CPU hours. We can notice that the cost of the different LES is from two to three orders of magnitude smaller than the cost of the corresponding DNS. The use of a turbulence model leads to an increase of the cost of approximately one third with respect to the corresponding no-model simulation. All the simulations have been performed on the Marconi cluster at CINECA. 576 cores

14
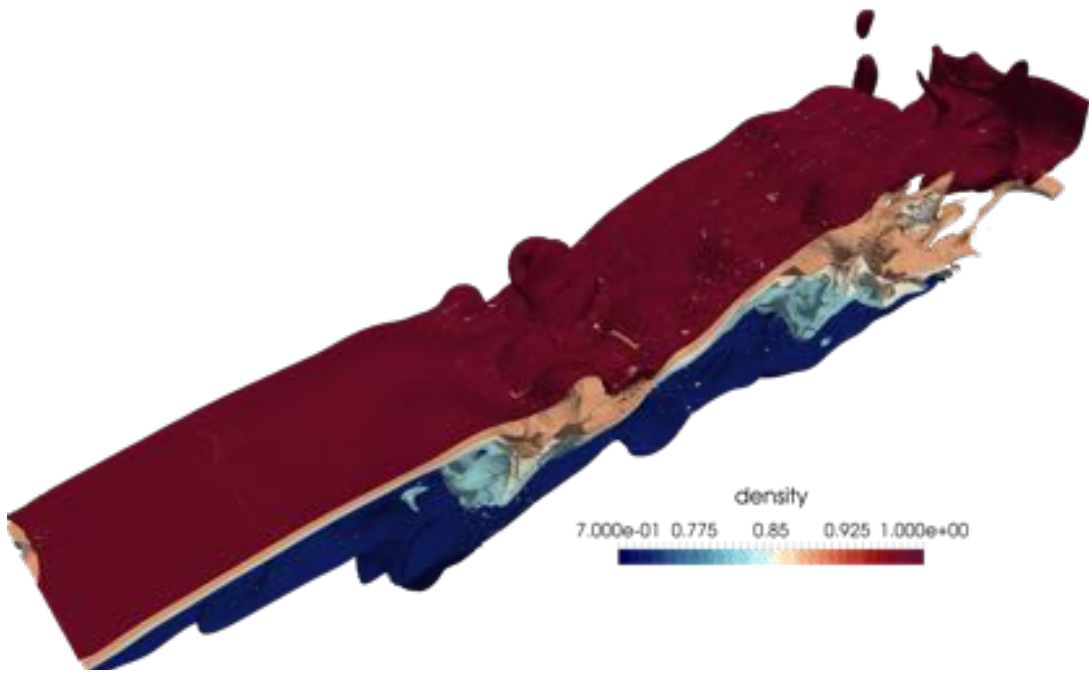
(a)
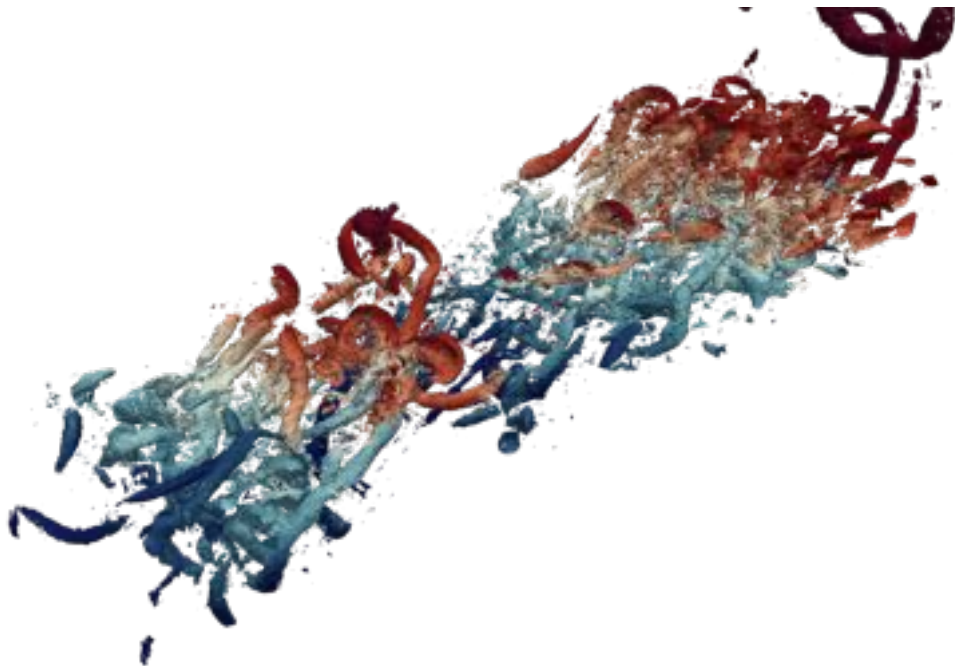
(b)

Figure 4: Isosurfaces at $t = 9$ for $Re = 6000$ (DNS) (a) density isosurfaces ($\rho = 0.72, 0.82, 0.85, 0.88, 0.98$). (b) $Q = 5$ isosurface (colored by density).

-	$Re = 3000$	$Re = 6000$
DNS	133900	133900
No model	750	5400
Smagorinsky	875	6300
Isotropic dyn.	1115	7800
Anisotropic dyn.	1117	7800

Table 5: Computational cost (CPU hours) for the different simulations.

have been employed for DNS and for the LES at $Re = 6000$, while 288 cores have been employed for the LES at $Re = 3000$.

Considering the $Re = 3000$ case, the comparison between the different LES density fields (figures 5(a), 6(a), 7(a), 8(a)) and the density field of the DNS (figure 2(a)), highlights the excessively dissipative behaviour of the Smagorinsky model. This fact is confirmed also by the comparison in terms of the $Q = 5$ isosurface. In particular we can see that the Smagorinsky model (figure 5(b)) and, to a lesser extent, also the anisotropic model (figure 7(b)) provide less turbulent structures with respect to the ones provided by the corresponding DNS (figure 2(b)).

Considering the $Re = 6000$ case at $t = 4$, if we look at the density profile obtained with the Smagorinsky model (figure 9(a)), we can notice that it is much smoother with respect to the DNS one, suggesting the fact that the Smagorinsky model could be too dissipative also in this case. This seems to be confirmed by the behaviour of the $Q = 20$ isosurface. If we compare the Smagorinsky one (figure 9(b)) with that of the DNS (figure 3(b)), we can see that the Smagorinsky model yields less turbulent structures with respect to the DNS. An improvement can be obtained employing dynamic models, both in the density and Q fields. In particular, figure 10(b) shows that the dynamic isotropic model provides many more turbulent structures with respect to the Smagorinsky model and allows the representation of the majority of the turbulent structures actually present in the DNS, even if the structures in the Q field appear more scattered. The same considerations can be made for the anisotropic dynamic model (see figures 11(a) and 11(b) for the density and $Q = 20$ isosurface respectively), even if a slightly more dissipative character is present, especially in the Q profile, with respect to the isotropic version. Notice that, even though the introduction of a dynamic model provides better results with respect to the Smagorinsky model, if we look at the profiles of density and Q obtained with the no-model LES (figures 12(a) and 12(b)) and we compare them with those ob-
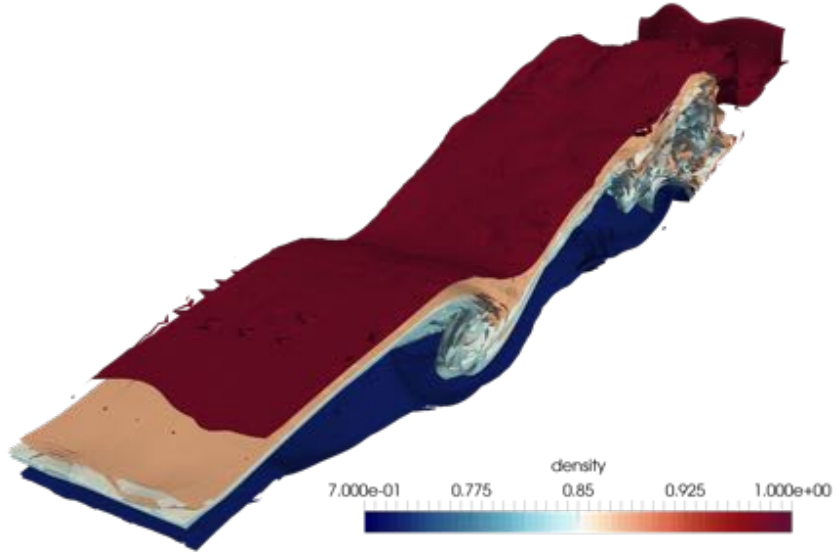
16
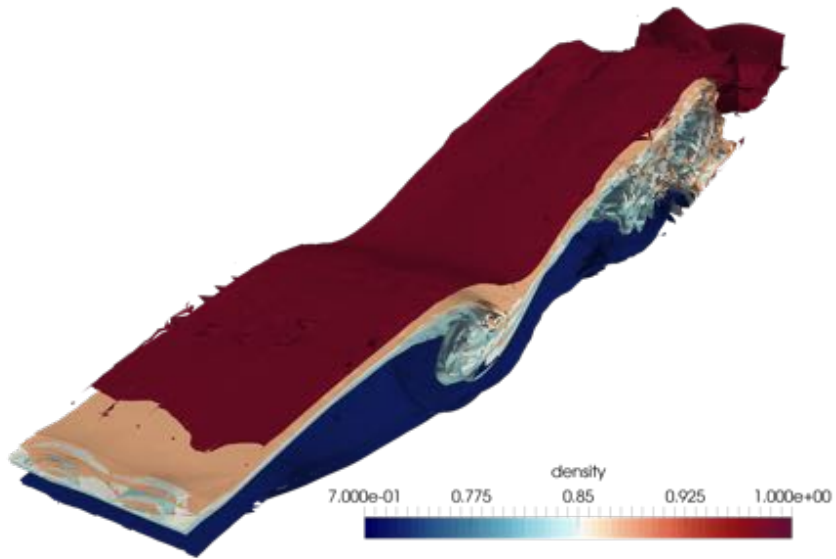
(a)

(b)

Figure 5: Isosurfaces at $t = 9$ for $Re = 3000$ (Smagorinksy model LES) (a) density isosurfaces ($\rho = 0.72, 0.82, 0.85, 0.88, 0.98$). (b) $Q = 5$ isosurface (colored by density).
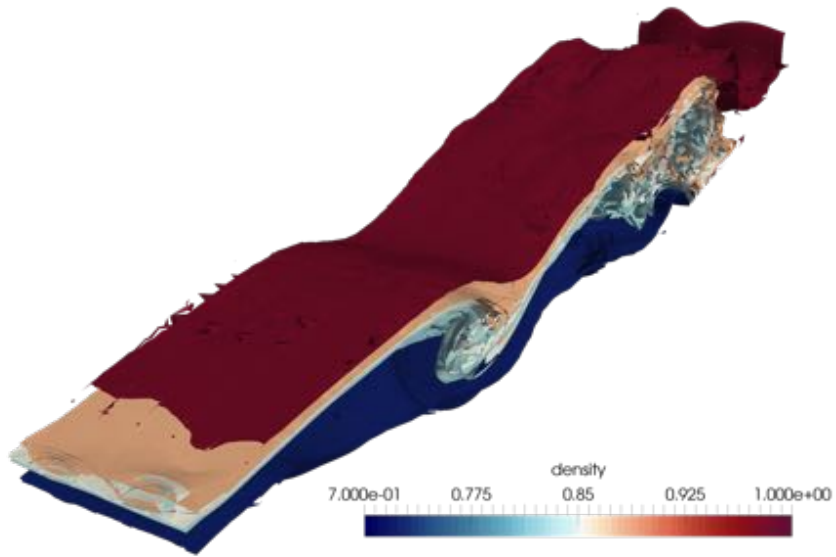
Figure 6: Isosurfaces at $t = 9$ for $Re = 3000$ (Isotropic dynamic model LES) (a) density isosurfaces ($\rho = 0.72, 0.82, 0.85, 0.88, 0.98$). (b) $Q = 5$ isosurface (colored by density).
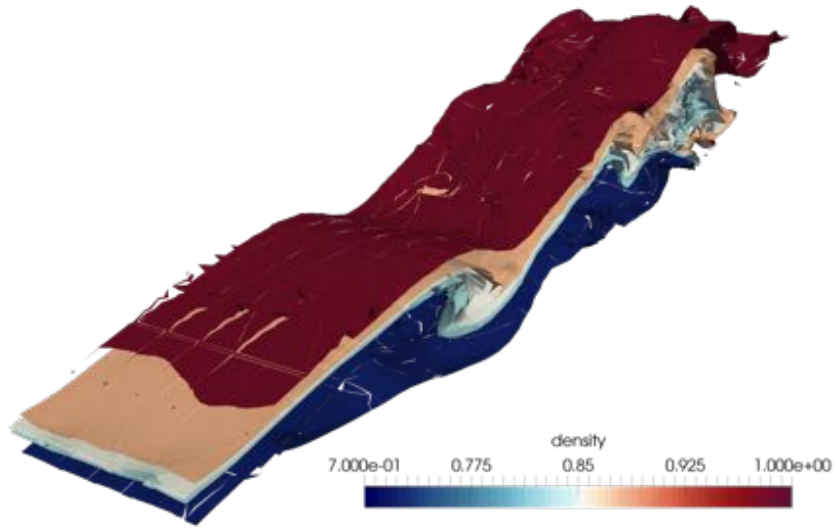
(a)

(b)

Figure 7: Isosurfaces at $t = 9$ for $Re = 3000$ (Anisotropic dynamic model LES) (a) density isosurfaces ($\rho = 0.72, 0.82, 0.85, 0.88, 0.98$). (b) $Q = 5$ isosurface (colored by density).
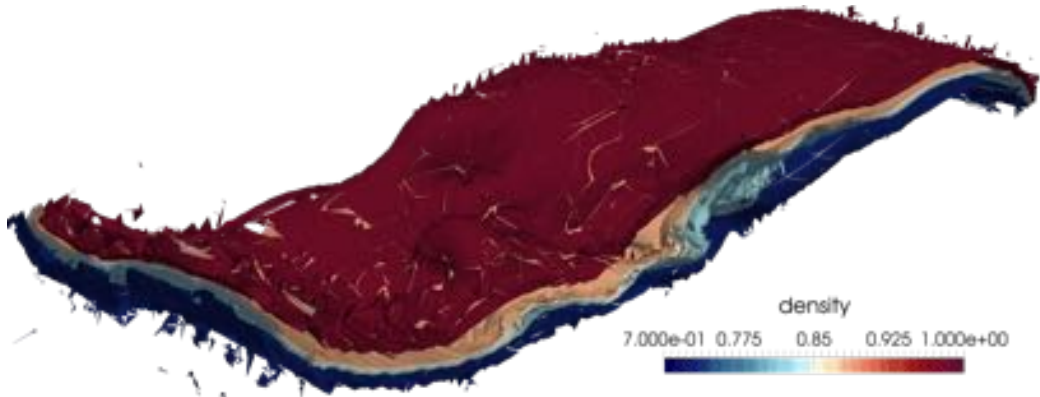
(a)

(b)

Figure 8: Isosurfaces at $t = 9$ for $Re = 3000$ (No model LES) (a) density isosurfaces ($\rho = 0.72, 0.82, 0.85, 0.88, 0.98$). (b) $Q = 5$ isosurface (colored by density).

tained with the dynamic models, it is not completely clear, from these instantaneous fields, if the introduction of a dynamic model leads to some improvement with respect to a simple no-model LES.

Considering then the $Re = 6000$ case at $t = 9$, if we compare figures 13(b), which represents the $Q = 5$ isosurface obtained with the Smagorinsky model, with the corresponding DNS field (figure 4(b)), we can confirm the fact that the Smagorinsky model is too dissipative. As for $t = 4$, an improvement can be obtained employing a dynamic model, both in terms of density and Q (see figures 14(b) and 15(b)). Notice that, at $t = 9$, some differences arise also between the dynamic models results and the no-model LES results. In particular, if we compare the $Q = 5$ field obtained with the isotropic dynamic model (figure 14(b)) and the anisotropic dynamic model (figure 15(b)) with the corresponding no-model field (figure 16(b)), we can see that the introduction of a model leads to the presence of more coherent turbulent structures with respect to the no-model case. However,it appears difficult to conclude, based only on analysis of the instantaneous fields, whether the introduction of a dynamic model actually leads to better results with respect to the no-model LES.

In order to allow for a fairer comparison of the LES results, we have also filtered the DNS results *a posteriori*, to see if additional informations on the performances of the different turbulence models can be obtained with respect to the comparison with the simple DNS Q field. Since it would have been quite cumbersome to post filter the DNS results considering the same polynomial degree ($p = 4$) and a coarser grid, we simply project the solution onto a lower dimensional polynomial space, in order to obtain a number of DOFs similar to the one of the $Re = 6000$ LES. In figure 17 we present the post-filtered DNS field for $Re = 6000$ and $t = 9$. If we compare this field to the corresponding DNS field (figure4(b)), we can notice that some small scale structures are less evident, as expected, even though the larger scale structure can still be identifed. However if we compare the DNS post filtered field of figure 17 with the corresponding LES fields of figures 13(b), 14(b), 15(b), 16(b), we cannot reach a satisfying conclusion about the performances of the different models.

In order to try to better discriminate the behaviour of the different LES models and their performances with respect to the DNS results, we consider the dissipated energy profiles as a function of time, computed as in equation (7) for the no-model case, the Smagorinsky model and the isotropic dynamic model, and as in equation (8) for the anisotropic dynamic model. The dissipated energy profiles are
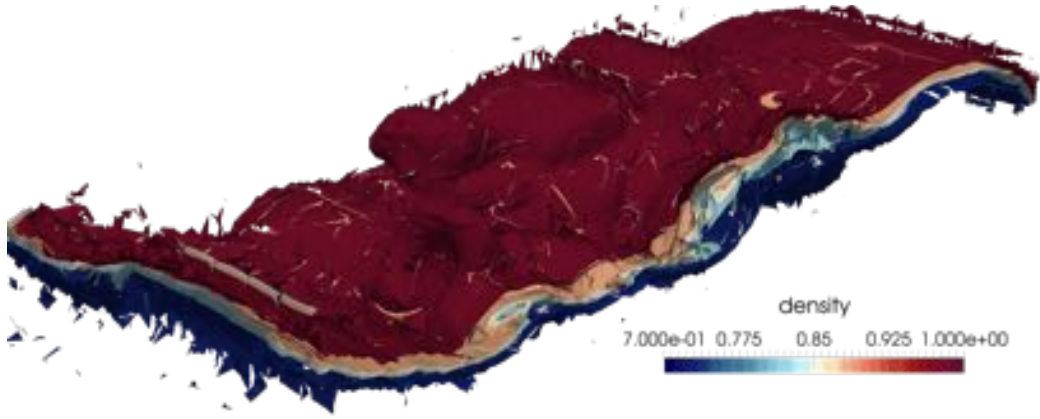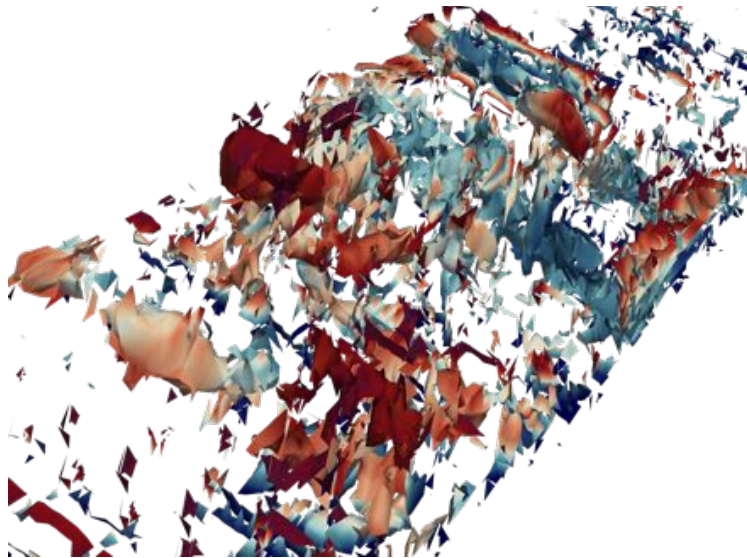
21

(a)

(b)

Figure 9: Isosurfaces at $t = 4$ for $Re = 6000$ (Smagorinsky model LES) (a) density isosurfaces ($\rho = 0.72, 0.82, 0.85, 0.88, 0.98$). (b) $Q = 20$ isosurface (colored by density).
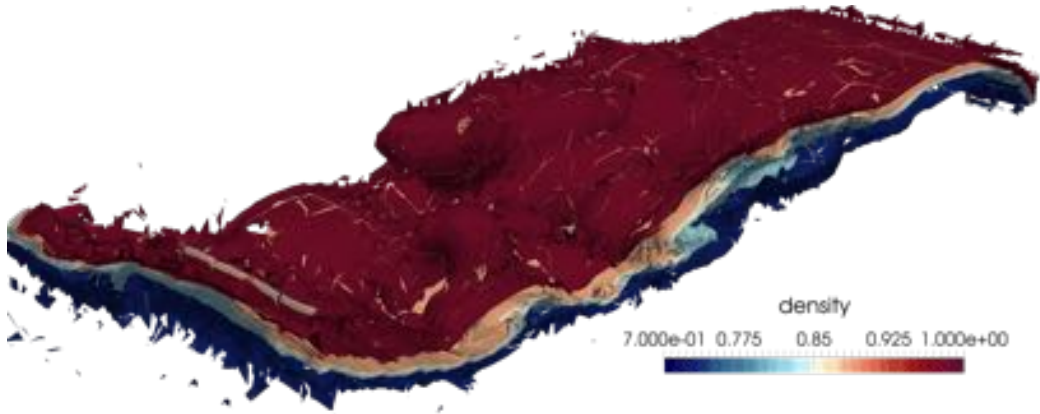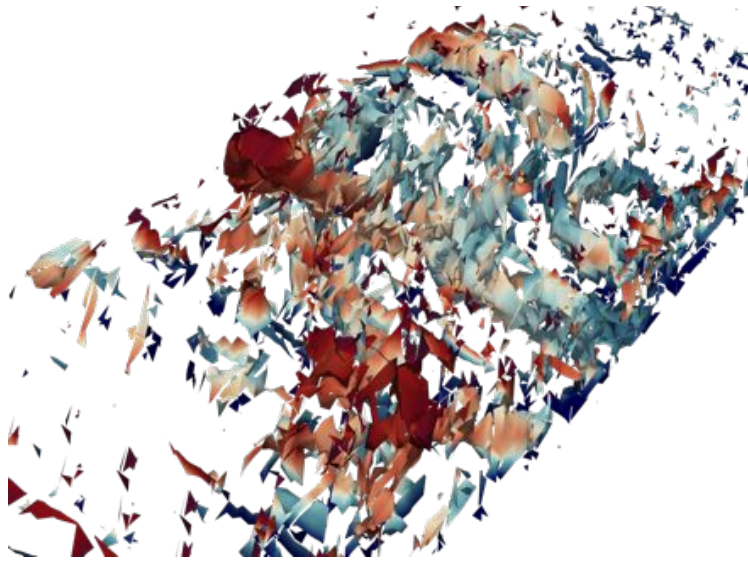
(a)

(b)

Figure 10: Isosurfaces at $t = 4$ for $Re = 6000$ (Isotropic dynamic model LES) (a) density isosurfaces ($\rho = 0.72, 0.82, 0.85, 0.88, 0.98$). (b) $Q = 20$ isosurface (colored by density).

(a)

(b)

Figure 11: Isosurfaces at $t = 4$ for $Re = 6000$ (Anisotropic dynamic model LES) (a) density isosurfaces ($\rho = 0.72, 0.82, 0.85, 0.88, 0.98$). (b) $Q = 20$ isosurface (colored by density).

(a)

(b)

Figure 12: Isosurfaces at $t = 4$ for $Re = 6000$ (No model LES) (a) density isosurfaces ($\rho = 0.72, 0.82, 0.85, 0.88, 0.98$). (b) $Q = 20$ isosurface (colored by density).

(a)

(b)

Figure 13: Isosurfaces at $t = 9$ for $Re = 6000$ (Smagorinsky model LES) (a) density isosurfaces ($\rho = 0.72, 0.82, 0.85, 0.88, 0.98$). (b) $Q = 5$ isosurface (colored by density).
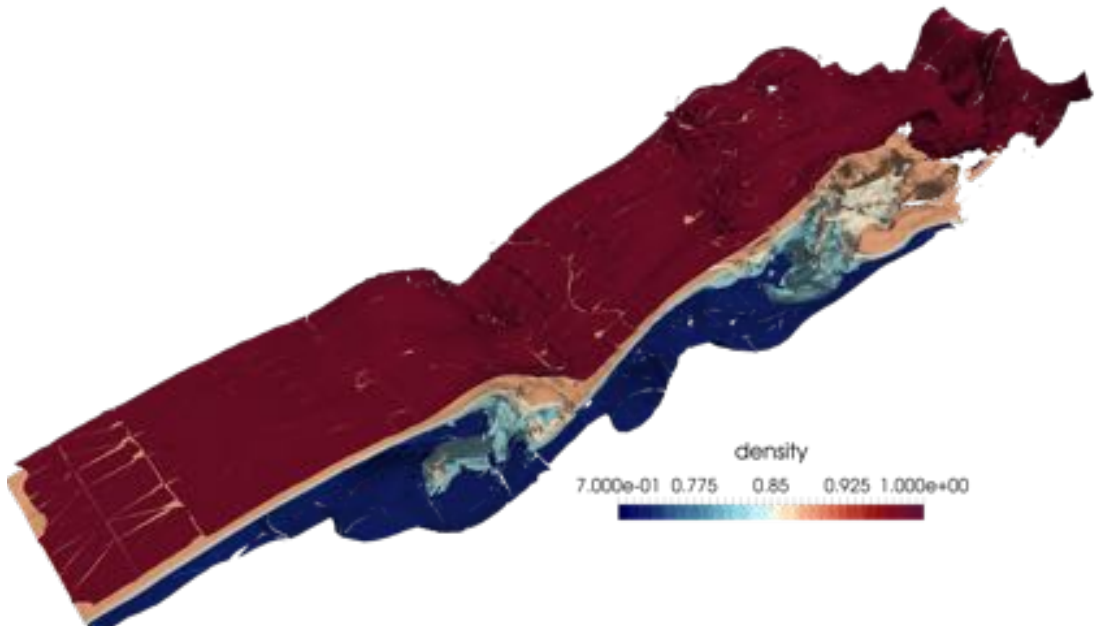
(a)
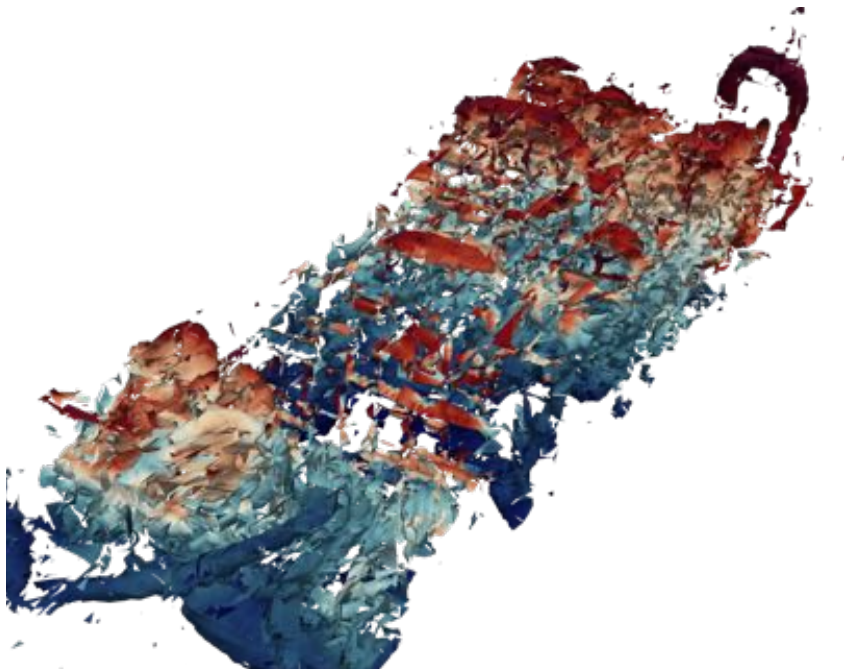
(b)

Figure 14: Isosurfaces at $t = 9$ for $Re = 6000$ (Isotropic dynamic model LES) (a) density isosurfaces ($\rho = 0.72, 0.82, 0.85, 0.88, 0.98$). (b) $Q = 5$ isosurface (colored by density).
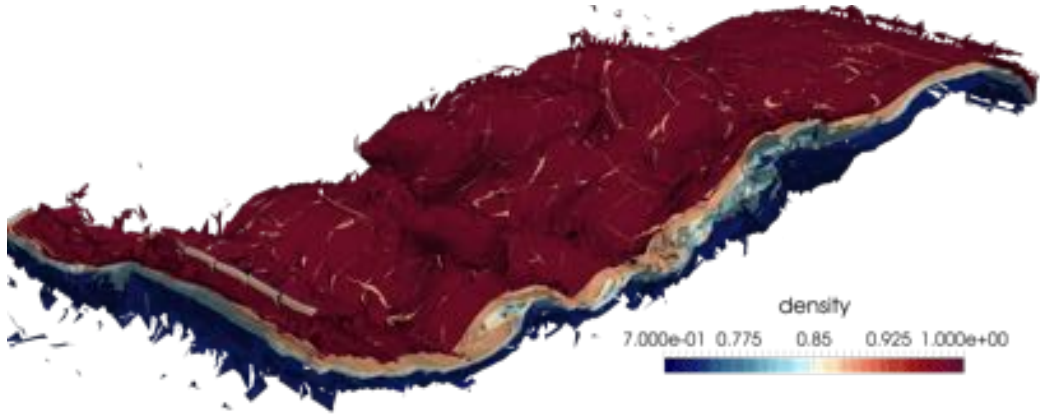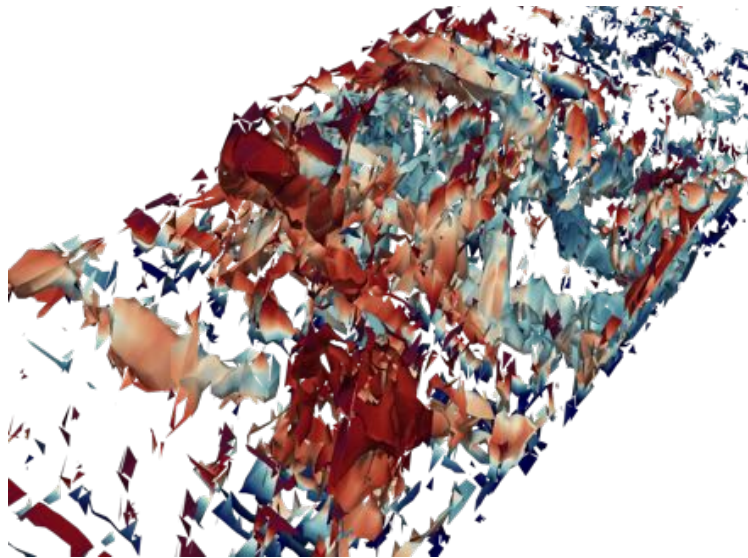
(a)

(b)

Figure 15: Isosurfaces at $t = 9$ for $Re = 6000$ (Anisotropic dynamic model LES) (a) density isosurfaces ($\rho = 0.72, 0.82, 0.85, 0.88, 0.98$). (b) $Q = 5$ isosurface (colored by density).
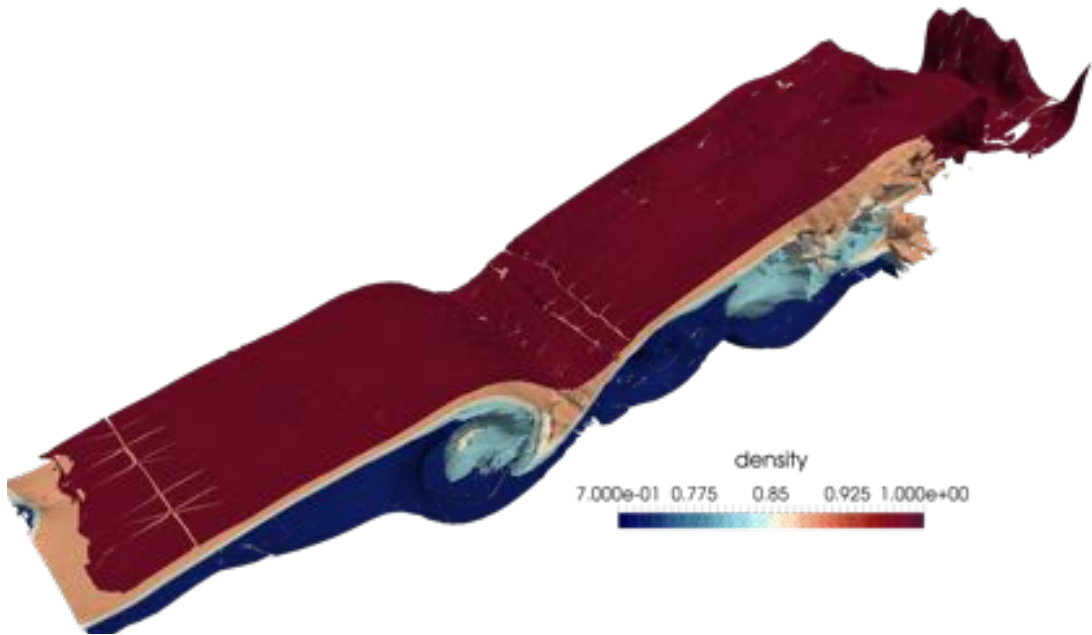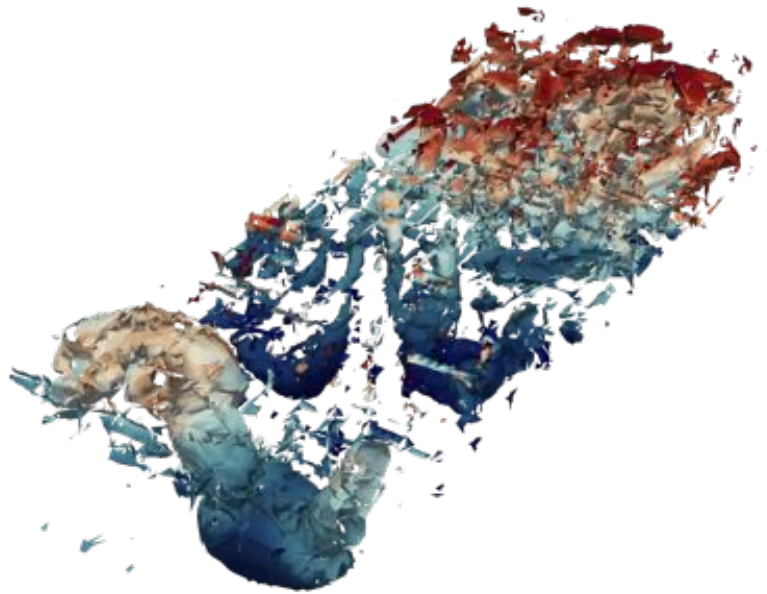
Figure 16: Isosurfaces at $t = 9$ for $Re = 6000$ (No model LES) (a) density isosurfaces ($\rho = 0.72, 0.82, 0.85, 0.88, 0.98$). (b) $Q = 5$ isosurface (colored by density).
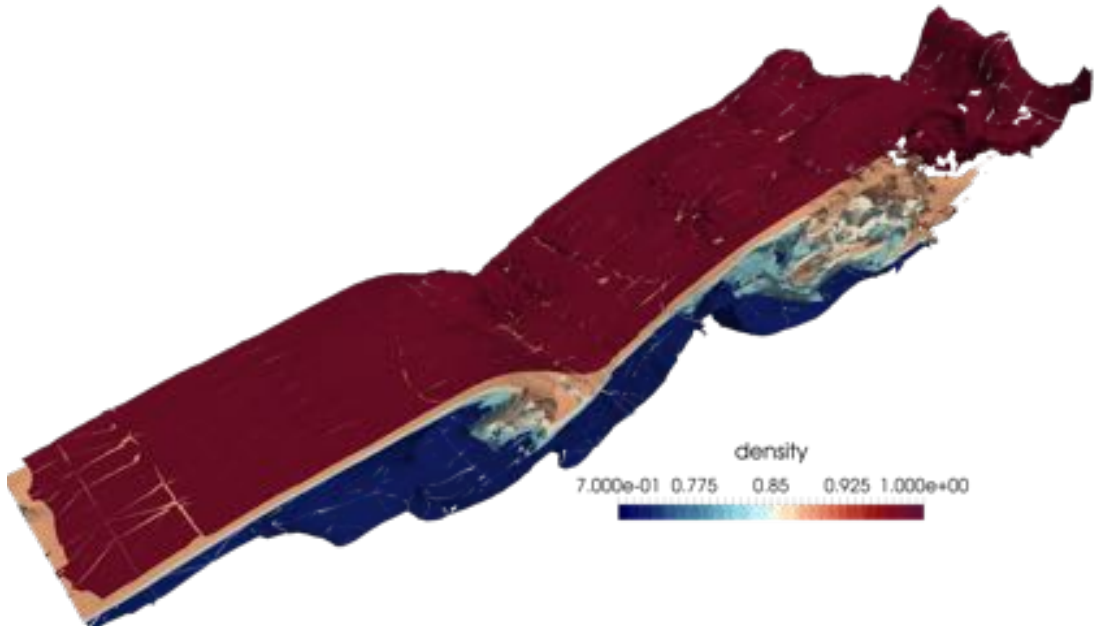
29

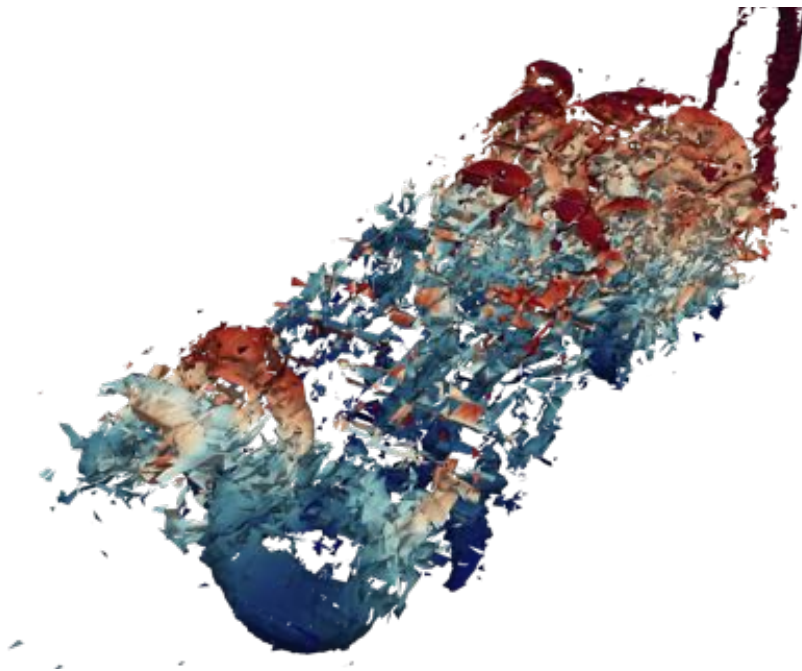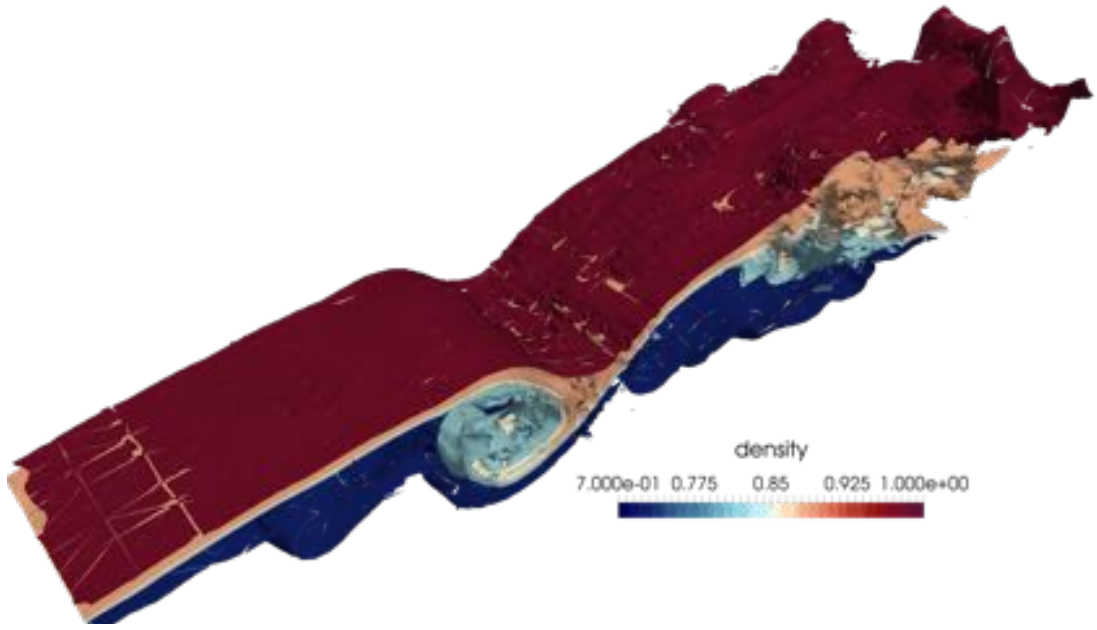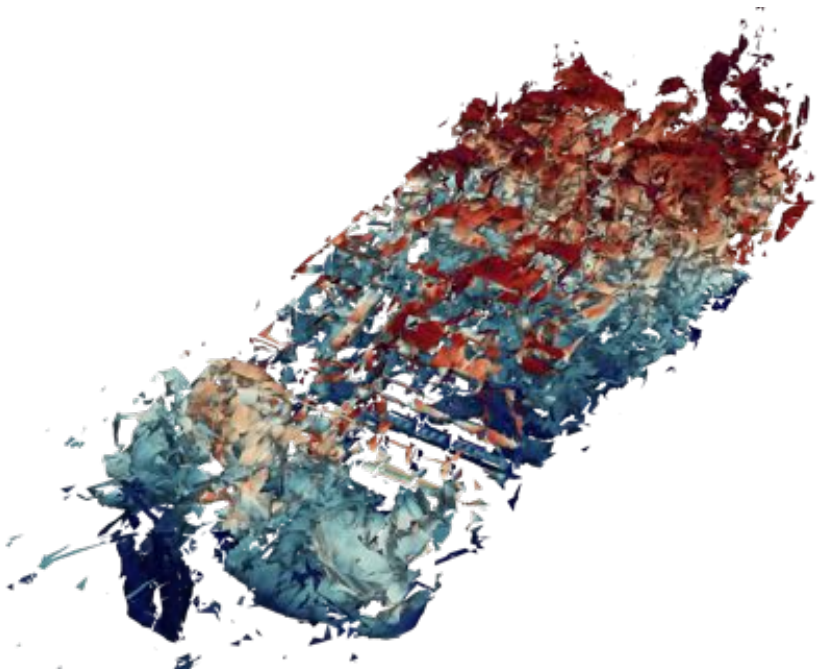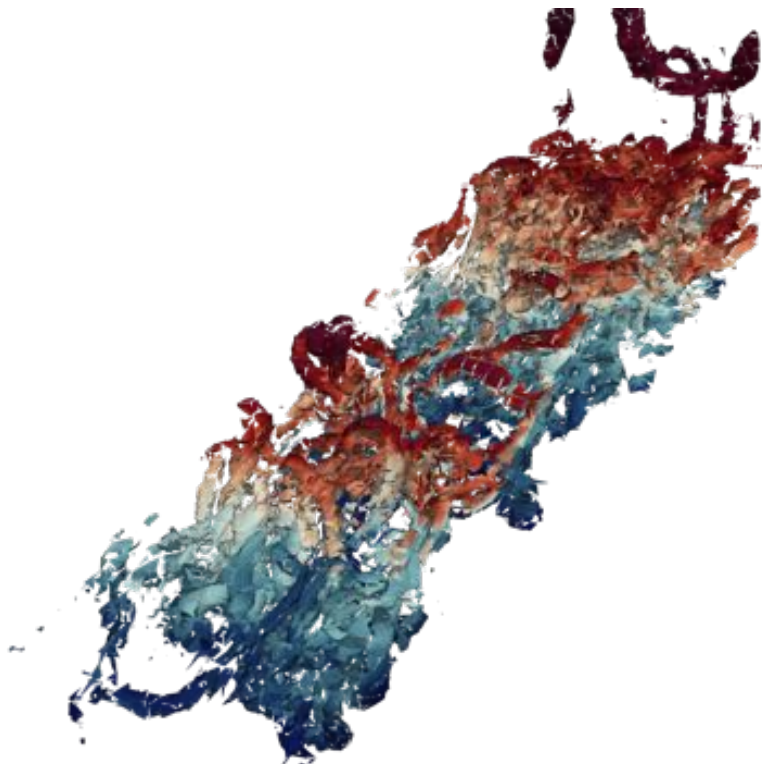Figure 17: Post-filtered DNS isosurfaces of $Q = 5$ at $t = 9$ for $Re = 6000$.

presented both for $Re = 3000$ and $Re = 6000$ cases in figure 18.

Concerning the $Re = 3000$ case (figure 18(a)), we can confirm the finding that the Smagorinsky model is far too dissipative: the dissipated energy obtained with the Smagorinsky model (cyan curve) is always greater than the DNS one (red curve). Considering the isotropic dynamic model (blue curve), we can notice that its dissipated energy profile is quite similar to the one provided by the no-model LES (green curve). Even if slightly more dissipative, the isotropic dynamic model is not able to recover the significant increase in the dissipated energy of the DNS starting from $t \simeq 7$. The anisotropic dynamic model (black curve) seems the one that provides the better results in terms of dissipated energy: the initial increasing in the DNS dissipated energy is quite well reproduced even though also the anisotropic dynamic model underestimates the energy dissipated in the DNS starting from $t \simeq 7$. The anisotropic dynamic model curve seems the one closer to the DNS profile also for $t > 22$.

Considering the $Re = 6000$ simulations (figure 18(b)), the behaviour of the Smagorinsky model (cyan curve) is always too dissipative, especially if we consider times $t > 14$. The no-model LES (green curve) and the LES obtained with the isotropic dynamic model (blue curve) present results with larger differences between each other than in the $Re = 3000$ case. The isotropic dynamic model presents a more dissipative behaviour with respect to the no model case. Both the isotropic and the anisotropic dynamic model (black curve) appear to provide the best results with a good reproduction of the initial ($t < 5$) and final ($t > 20$) DNS dissipated energy profile, even if they are not able to capture the behaviour of the DNS dissipated energy for $t \in [5, 20]$.

As an additional diagnostic, we have also computed the temporal evolution of the maximum and minimum values of the ratio ν_{sgs}/ν between the subgrid-scale viscosity ν_{sgs} and the molecular viscosity ν over the whole domain (see figure 19). Figure 19(a) corresponds to the $Re = 3000$ case, while figure 19(b) to Reynolds $Re = 6000$. Solid lines correspond to the different viscosities related to the anisotropic model (for a three-dimensional problem we have six different components of the tensor of the subgrid viscosities, see appendix A.3), the blue dotted line corresponds to the isotropic dynamic model, while the cyan dotted curve refers to the Smagorinsky model. The anisotropic dynamic model provides the larger peak values, the isotropic dynamic model intermediate peak values while the Smagorinsky model the lowest values. We can notice that greater differences are present between the peak values of the isotropic and

31
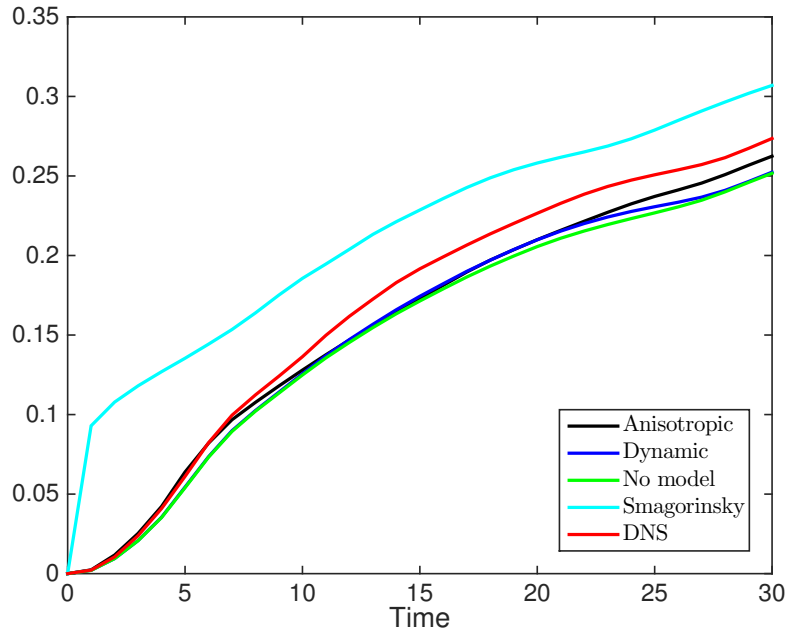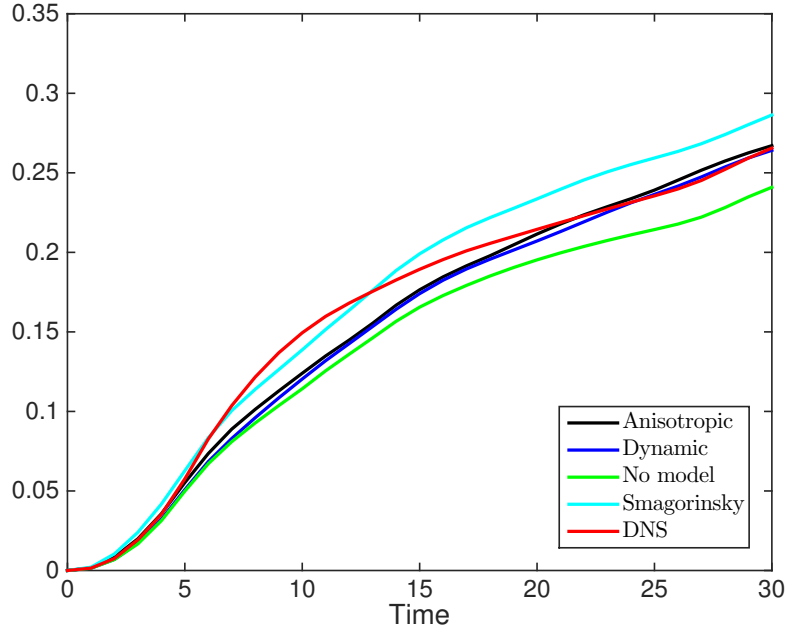
Figure 18: Dissipated energy as a function of time. (a) $Re = 3000$. (b) $Re = 6000$.

32

the ansotropic dynamic models in the Reynolds $Re = 3000$ case (figure 19(a)), with respect to the $Re = 6000$ case. This probably means that, in the $Re = 6000$ case (figure 19(b)), the flow has a more isotropic character than in the $Re = 3000$ case. Notice that, for both the $Re = 3000$ and the $Re = 6000$ case and especially for the anisotropic dynamic model, the maximum values of the ratio ν_{sgs}/ν tend to a constant value toward the end of the simulation. This trend is evident also for the Smagorinsky and the dynamic isotropic models even if larger amplitude oscillations are present.

A similar behaviour is obtained if we consider the minimum values of the ratio ν_{sgs}/ν (figure 20): as for the maximum values, figure 20(a) refers to $Re = 3000$ while figure 20(b) to $Re = 6000$. We have not reported the curve relative to the Smagorinsky model since it presents peak values nearly equal to zero, because of the fact that the Smagorinsky model is purely dissipative and does not allow backscatter. The dynamic model (blue dotted curve) presents, in absolute value, smaller negative peak values with respect to the anisotropic model (solid curves). Also in this case, the difference between the peak values provided by the isotropic and the anisotropic dynamic models is greater in the $Re = 3000$ case. Even if the Smagorinsky model appears to be more dissipative with respect to the other LES models if we look at the density isosurfaces and at the dissipated energy profiles, its subgrid viscosity peak values are lower. The Smagorinsky model is, in some sense, less selective with respect to the isotropic and anisotropic dynamic models and introduces a smaller, but more distributed dissipation. This last statement can be checked representing, at a fixed instant of time, the field of the ratio ν_{sgs}/ν for the different turbulence models. In figure 21, which refers to the $Re = 3000$ simulation at $t = 4$, we represent in red the portion of the mesh in which the ratio ν_{sgs}/ν takes values greater than 0.3 for the Smagorinsky model (figure 21(a)), the isotropic dynamic model (figure 21(b)) and the anisotropic dynamic model (figure 21(c)). Notice that for the anisotropic dynamic model the 22 component of ν_{sgs}/ν is represented, while the other components present similar patterns. If we compare the fields provided by the Smagorinsky model and by the isotropic dynamic model, we can easily see that the portion of the mesh, for which the condition $\nu_{sgs}/\nu > 0.3$ is verified, is much smaller in the isotropic dynamic model case. For the different components of ν_{sgs}/ν, when employing the anisotropic dynamic model, the condition ν_{sgs}/ν is verified for a greater portion of the mesh with respect to the isotropic dynamic model case. However, the overall dissipation is smaller than in the Smagorinsky model case (see figure 18): this is due to the
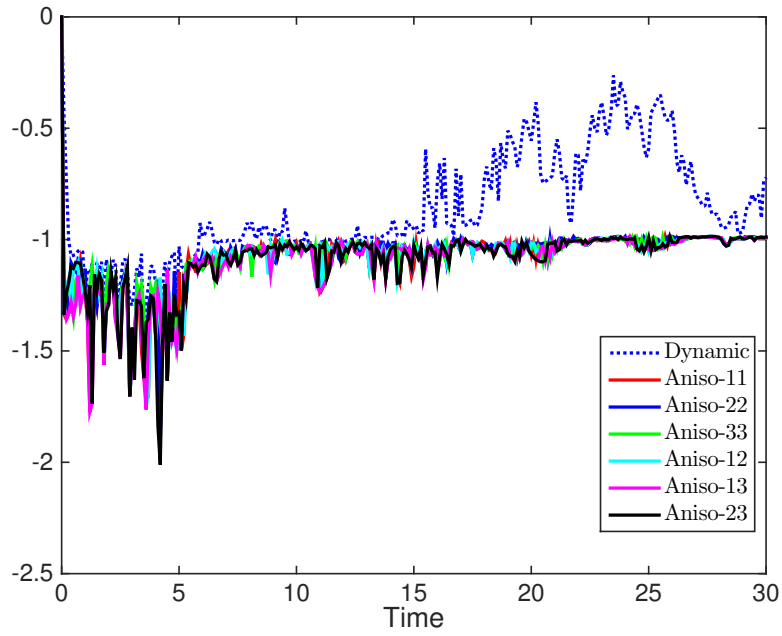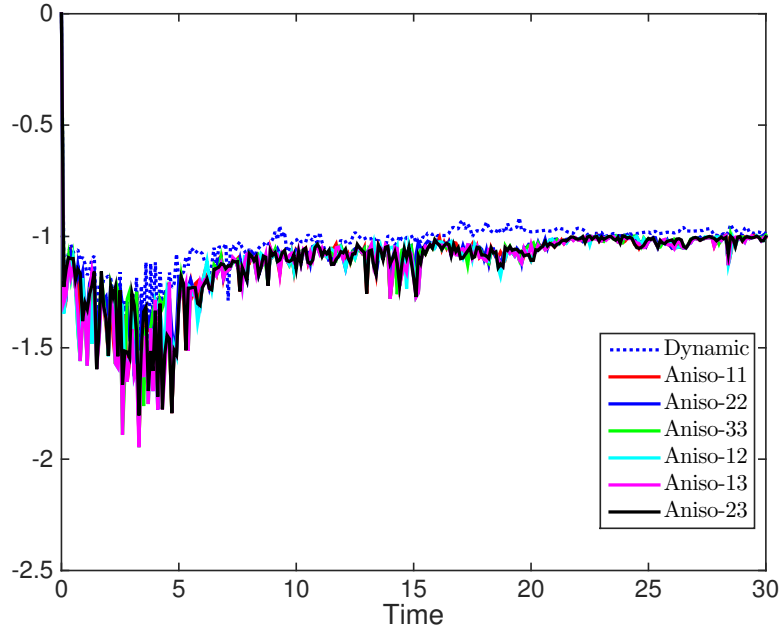
33
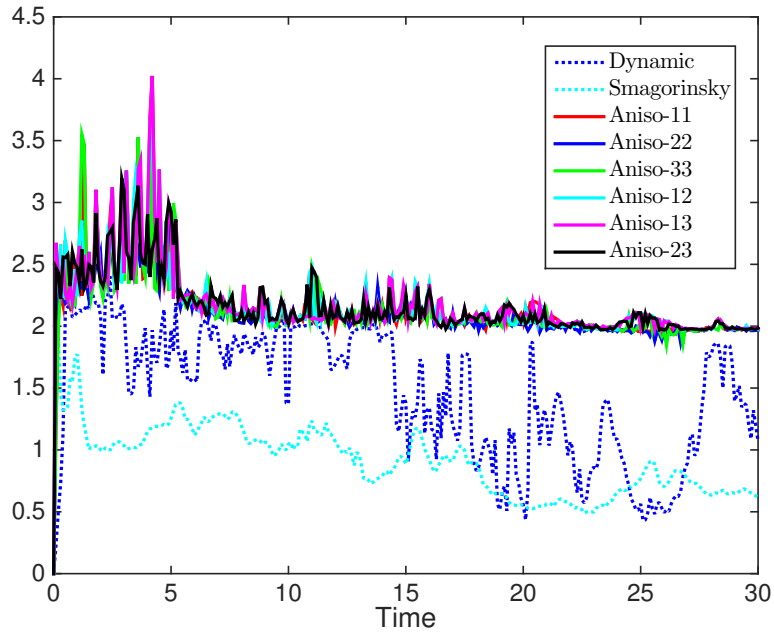
(a)
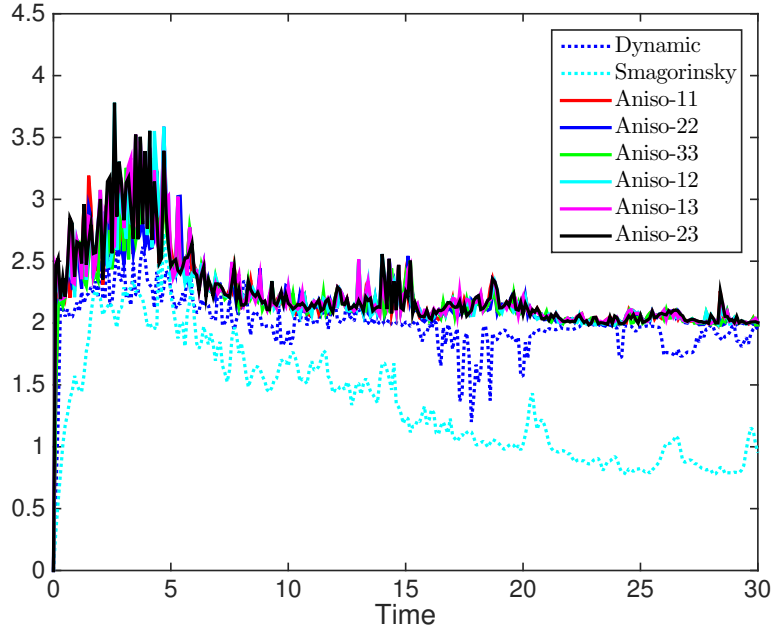
(b)

Figure 19: Maximum value over the whole domain of ν_{sgs}/ν, as a function of time. (a) $Re = 3000$. (b) $Re = 6000$.

Figure 20: Minimum value value over the whole domain of ν_{sgs}/ν, as a function of time. (a) $Re = 3000$. (b) $Re = 6000$.

presence of backscatter, which is absent in the Smagorinsky model case. If we look at figure 22, where the part of the mesh in which the condition $\nu_{sgs}/\nu < -0.3$ is verified is represented in blue, we can notice that for the anisotropic dynamic model (figure 22(b)) this condition is satisfied for a large portion of the mesh, indicating that this model well reproduces the backscatter phenomenon in the shear layer at the interface between the two densities. Notice that the presence of consistent backscatter in shear layers has already been highlighted for example in [31]. The isotropic dynamic model (figure 22(a)) introduces much less backscatter with respect to the anisotropic counterpart.

As in [30] and [29], we now perform a comparison between the different LES models employing the Reference Potential Energy (RPE), introduced at the beginning of the present section. In figure 23, we show the RPE profiles as a function of time, obtained with the DNS and with different turbulence models. Figure 23(a) refers to $Re = 3000$, while figure 23(b) to $Re = 6000$. In the $Re = 3000$ case, we can notice that the Smagorinsky model (cyan curve) has the worst performance, with a significant overestimation of the reference potential energy. The RPE obtained with no model (green curve) and with the isotropic dynamic model (blue curve) are similar to each other and also quite similar to the DNS RPE. The anisotropic dynamic model (black curve) provides a slight underestimation of the RPE profile.

If we consider the $Re = 6000$ case, we can notice that, after an initial slight underestimation of the DNS RPE, starting from $t > 15$, the RPE provided by the anisotropic dynamic model (black curve) is very similar to the DNS RPE (red curve), while the $RPEs$ provided by the no-model (green curve) and the isotropic dynamic model (blue curve) are very close and greater than the DNS RPE. The introduction of the Smagorinsky model (cyan curve) leads to a deterioration of the results in term of RPE with respect to the no-model simulation, with an overestimation of the RPE.

Notice that the RPE results presented in figure 23, are obtained plotting the RPE every non-dimensional time unit. If we present the plot of the RPE, for example obtained with the no model LES in the $Re = 3000$ case, representing the RPE every 0.1 non-dimensional time units, we can notice that small-period oscillations appear (see figure 24). We can easily see that the period of these oscillations is approximately equal to 1 non-dimensional time unit. It can also be observed that the time employed by an acoustic wave to cover the length of the domain from 0 to L and then back

(a)

(b)

(c)

Figure 21: Portion of the domain (in red), on the plane $y = 0.5$, in which the condition $\nu_{sgs}/\nu > 0.3$ is satisfied for $Re = 3000$ at $t = 4$. (a) Smagorinsky model. (b) Isotropic dynamic model. (c) Anisotropic dynamic model (component 22 of ν_{sgs}/ν).

(a)

(b)

Figure 22: Portion of the domain (in blue), on the plane $y = 0.5$, in which the condition $\nu_{sgs}/\nu < -0.3$ is satisfied for $Re = 3000$ at $t = 4$. (a) Isotropic dynamic model. (b) Anisotropic dynamic model (component 22 of ν_{sgs}/ν).
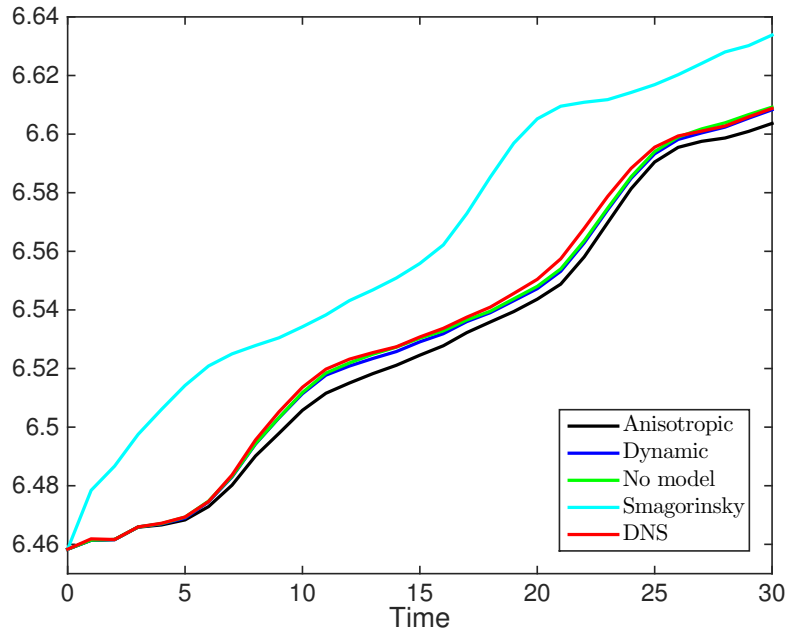
(a)
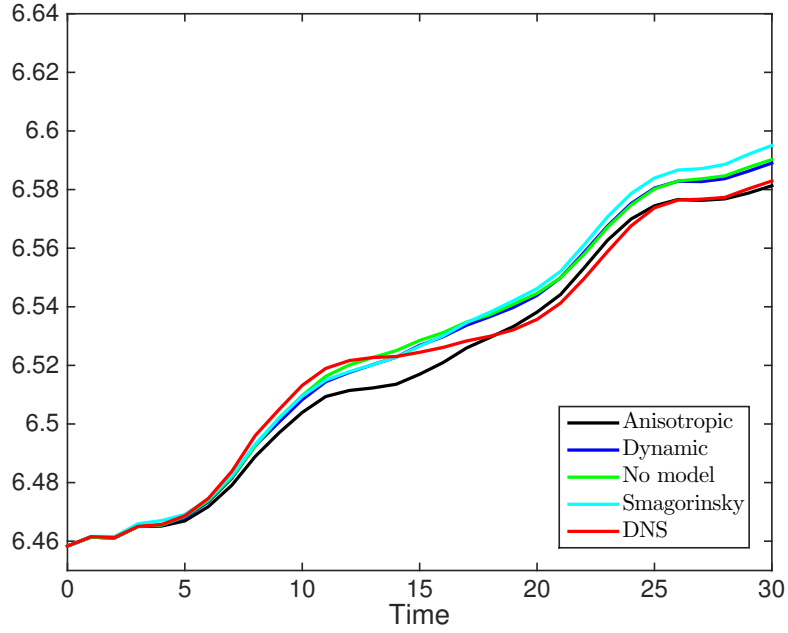
(b)

Figure 23: Reference Potential Energy (RPE) as a function of time. (a) $Re = 3000$. (b) $Re = 6000$.
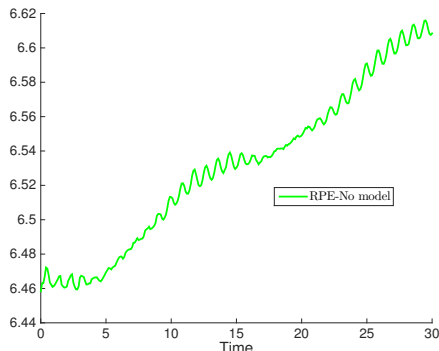
Figure 24: RPE as a function of time for $Re = 3000$, obtained from the no model LES sampling the solution each 0.1 non-dimensional time unit.

from L to 0 is given by:

$$T_{2L} = 2LMa = 2L0.1 = 1, \qquad (24)$$

in non-dimensional time units. As a consequence, we believe that the small period oscillations are caused by the fact that we are considering slightly compressible simulations in which acoustic perturbations can be induced by the abrupt start of the lock exchange test. Indeed, these small period oscillations are instead absent in the incompressible simulations available in the literature. The acoustic perturbations have probably an influence on the computation of the probability density function $P(\rho)$, employed in order to derive the RPE. We believe however that the presence of these small-period oscillations does not affect the general behaviour of the RPE, so that the comparison of the results obtained with different turbulence models in terms of RPE is significant.

Concluding, the Smagorinsky model has the worst performance, with respect to both the instantaneous fields and the more quantitative diagnostics, as the dissipated energy and the RPE. Considering the other turbulence models, no model is able to correctly reproduce the large increase in the dissipated energy which is present in the DNS results. However, the anisotropic dynamic model is the one that, in particular in the $Re = 6000$ case, appears to provide the best results in terms of the dissipated energy. Concerning the RPE, in the $Re = 3000$ case, the no-model and the isotropic dynamic model $RPEs$ are quite similar and also similar to the DNS one. The anisotropic dynamic model provides a slight underestimation of the RPE in the $Re = 3000$ case and also at the beginning of the $Re = 6000$ simulation, but it appears to give the best results, especially in the $Re = 6000$ case, toward the end of the simulation.

40

6 Conclusions and future perspectives

We have carried out three-dimensional simulations of non-Boussinesq gravity currents in the lock-exchange configuration. First, three-dimensional DNS in the non-Boussinesq regime were performed at two different Reynolds numbers. In the LES experiments we have employed the Smagorinsky model, the isotropic dynamic model and the anisotropic dynamic model, together with a no model run. The considered diagnostics (instantaneous density and Q-criterion fields, time evolution of the dissipated energy and of the Reference Potential Energy) allow to confirm the fact that the Smagorinsky model is too dissipative. Concerning the other models, the dynamic models (isotropic and anisotropic) seem to provide the best results in terms of dissipated energy and Reference Potential Energy, with slightly better results provided by the anisotropic dynamic model.

Concerning the possible future developments, a first goal is the implementation of new turbulence models for variable density flows, based on the work [18] and on the preliminary *a priori* analysis reported in [10], in the same configuration as employed for the LES carried out here, in order to see if an improvement of the results can be obtained with respect to the results obtained with the turbulence models already tested.

From a more numerical point of view, we also plan to implement a semi-implicit time integration scheme, following [21], [39] and [15], in order to improve the computational efficiency, in particular when considering very low Mach number flows. In order to improve efficiency, we then plan to perform $p-$adaptive simulations following [40], [39] and [38].

A Subgrid-scale models

All the subgrid models we describe are built on the Boussinesq hypothesis [32], which affirms that the energy transfer mechanism from the resolved scales to the subgrid scales is analogous to the molecular diffusion phenomenon, represented by the diffusion term. A term which has the same mathematical structure as the molecular diffusion term is then introduced in the NS equations to model the subgrid stress tensor. More precisely, similarly to the molecular viscosity, which is related to the magnitude of the molecular diffusion, a subgrid-scale viscosity is introduced in order to set the magnitude of the energy transfer between the resolved and the unresolved scales.

A.1 The Smagorinsky model

In the Smagorinsky subgrid model, first introduced in [34], the deviatoric part of the subgrid stress tensor τ_{ij} in (2) is modelled by a scalar turbulent viscosity ν^{sgs}:

$$\tau_{ij} - \frac{1}{3}\tau_{kk}\delta_{ij} = -\overline{\rho}\nu^{\text{sgs}}\widetilde{\mathcal{S}}_{ij}^{d}, \qquad (25a)$$

$$\nu^{\text{sgs}} = C_S^2\Delta^2|\widetilde{\mathcal{S}}|, \qquad (25b)$$

where C_S is the Smagorinsky constant (equal to 0.1 in the present work), $|\widetilde{\mathcal{S}}|^2 = \frac{1}{2}\widetilde{\mathcal{S}}_{ij}\widetilde{\mathcal{S}}_{ij}$ and Δ is the filter scale. The isotropic part of the subgrid stress tensor can be modelled as:

$$\tau_{kk} = C_I\overline{\rho}\Delta^2|\widetilde{\mathcal{S}}|^2. \qquad (26)$$

The subgrid temperature flux (4b) is set proportional to the resolved temperature gradient:

$$Q_i^{\text{sgs}} = -\frac{1}{Pr^{\text{sgs}}}\overline{\rho}\nu^{\text{sgs}}\partial_i\widetilde{T}, \qquad (27)$$

where Pr^{sgs} is a subgrid Prandtl number. The term $\tau(u_i, u_k, u_k)$ in the subgrid turbulent diffusion flux J_j^{sgs} (4c) is neglected by analogy with RANS leading to:

$$J_i^{\text{sgs}} \approx 2\widetilde{u}_k\tau_{ik} + \widetilde{u}_i\tau_{kk}. \qquad (28)$$

A.2 The Germano dynamic model

In the Germano dynamic model [19], the terms C_S and C_I of the Smagorinsky model are no more chosen *a-priori* for the whole domain, but are computed dynamically as functions of the resolved field. The deviatoric part of the stress tensor is the same as in the Smagorinsky model:

$$\tau_{ij} - \frac{1}{3}\tau_{kk}\delta_{ij} = -\overline{\rho}C_S\Delta^2|\widetilde{\mathcal{S}}|\widetilde{\mathcal{S}}_{ij}^{d}. \qquad (29)$$

The coefficient C_S is dynamically computed by introducing a test filter operator $\widehat{\cdot}$ associated to a spatial scale $\widehat{\Delta}$ which is larger than the spatial scale Δ related to the filter $\overline{\cdot}$. A Favre filter (see equation (1)), denoted with $\breve{\cdot}$, is associated to the test filter through the following Favre decomposition:

$$\widehat{\rho f} = \widehat{\rho}\breve{f}. \qquad (30)$$

If the test filter $\hat{\cdot}$ is applied to the momentum equation (2b) we obtain:

$$\partial_t \left(\widehat{\bar{\rho} \breve{u}_i} \right) + \partial_j \left(\widehat{\bar{\rho} \breve{u}_i \breve{u}_j} \right) + \partial_i \widehat{\bar{p}} - \partial_j \widehat{\sigma}_{ij} = -\partial_j \left(\widehat{\tau}_{ij} + \mathcal{L}_{ij} \right), \qquad (31)$$

where

$$\mathcal{L}_{ij} = \widehat{\overline{\rho} \widetilde{u}_i \widetilde{u}_j} - \widehat{\bar{\rho}} \breve{\widetilde{u}}_i \breve{\widetilde{u}}_j \qquad (32)$$

is the Leonard stress tensor. If we assume that the deviatoric part of the term at the right-hand side of equation (31) can be modelled using an eddy viscosity model and we employ a least square approach as described in [1], we obtain for the Smagorinsky constant C_S the following expression:

$$C_S = \frac{\mathcal{L}_{ij}^d \mathcal{R}_{ij}}{\mathcal{R}_{kl} \mathcal{R}_{kl}}, \qquad (33)$$

where $\mathcal{R}_{kl} = \widehat{\bar{\rho} \Delta^2 |\widetilde{\mathcal{S}}| \widetilde{\mathcal{S}}_{kl}^d} - \widehat{\bar{\rho}} \widehat{\Delta}^2 |\breve{\widetilde{\mathcal{S}}}| \breve{\widetilde{\mathcal{S}}}_{kl}^d$.

The same dynamic procedure is applied to the isotropic component of the subgrid stress tensor:

$$\tau_{kk} = C_I \bar{\rho} \Delta^2 |\widetilde{\mathcal{S}}|^2, \qquad (34)$$

where the C_I coefficient is determined by:

$$C_I = \frac{\widehat{\mathcal{L}_{kk}}}{\widehat{\bar{\rho}} \widehat{\Delta}^2 |\breve{\widetilde{\mathcal{S}}}|^2 - \widehat{\bar{\rho} \Delta^2 |\widetilde{\mathcal{S}}|^2}}. \qquad (35)$$

A similar approach is proposed for the subgrid terms in the energy equation. The subgrid heat flux is defined as:

$$Q_i^{\text{sgs}} = -\bar{\rho} \Delta^2 |\widetilde{\mathcal{S}}| C_Q \partial_i \widetilde{T}. \qquad (36)$$

The coefficient C_Q in equation (36) is then obtained as:

$$C_Q = \frac{\mathcal{L}_i^Q \mathcal{R}_i^Q}{\mathcal{R}_k^Q \mathcal{R}_k^Q}, \qquad (37)$$

with $\mathcal{R}_i^Q = \widehat{\bar{\rho} \Delta^2 |\widetilde{\mathcal{S}}| \partial_i \widetilde{T}} - \widehat{\bar{\rho}} \widehat{\Delta}^2 |\breve{\widetilde{\mathcal{S}}}| \partial_i \breve{\widetilde{T}}$ and $\mathcal{L}_i^Q = \widehat{\overline{\rho} \widetilde{u}_i \widetilde{T}} - \widehat{\bar{\rho}} \breve{\widetilde{u}}_i \breve{\widetilde{T}}$ temperature Leonard flux.

Concerning the subgrid turbulent diffusion flux, the term $\tau(u_i, u_k, u_k)$ in equation (4c) is not neglected as in the Smagorinsky model but a scale similarity model is assumed and this term is approximated as a subgrid kinetic energy flux:

$$\tau(u_i, u_k, u_k) \approx \overline{\rho \widetilde{u_i u_k u_k}} - \overline{\rho \widetilde{u}_i \widetilde{u_k u_k}}. \qquad (38)$$

The subgrid kinetic energy flux in equation (38) $\tau(u_i, u_k, u_k)$ is then modeled as a function of the gradient of the resolved kinetic energy:

$$\tau(u_i, u_k, u_k) = -\overline{\rho}\Delta^2|\widetilde{\mathcal{S}}|C_J\partial_i\left(\frac{1}{2}\widetilde{u}_k\widetilde{u}_k\right).\qquad(39)$$

Introducing the kinetic energy Leonard flux:

$$\mathcal{L}_i^J = \widehat{\overline{\rho}\widetilde{u}_i\widetilde{u}_k\widetilde{u}_k} - \widehat{\overline{\rho}}\breve{\widetilde{u}}_i\breve{\widetilde{u}}_k\breve{\widetilde{u}}_k,\qquad(40)$$

the value of the constant C_J is computed as:

$$C_J = \frac{\mathcal{L}_i^J\mathcal{R}_i^J}{\mathcal{R}_k^J\mathcal{R}_k^J},\qquad(41)$$

where $R_i^J = \overline{\rho}\Delta^2|\widetilde{\mathcal{S}}|\widehat{\partial_i\left(\frac{1}{2}\widetilde{u}_k\widetilde{u}_k\right)} - \widehat{\overline{\rho}}\widehat{\Delta^2}|\breve{\widetilde{\mathcal{S}}}|\partial_i\left(\frac{1}{2}\breve{\widetilde{u}}_k\breve{\widetilde{u}}_k\right)$. Considering equations (4c) and (39), the final expression for the subgrid turbulent diffusion flux is:

$$J_i^{\text{sgs}} = -\overline{\rho}\Delta^2|\widetilde{\mathcal{S}}|C_J\partial_i\left(\frac{1}{2}\widetilde{u}_k\widetilde{u}_k\right) + 2\widetilde{u}_k\tau_{ik} + \widetilde{u}_i\tau_{kk},\qquad(42)$$

where C_J is given by equation (41). It is important to point out that all the dynamic coefficients are averaged over each element in order to avoid numerical instabilities; moreover, since the dynamic model allows backscattering, a clipping procedure is applied to ensure that the total dissipation, resulting from both the viscous and the subgrid stresses, is positive.

A.3   The anisotropic dynamic model

We describe here the anisotropic dynamic model introduced in [2] and extended to the compressible flows case in [1]. The main characteristic of this anisotropic model is that it overcomes the limitation of the alignment between the subgrid flux tensors and the corresponding gradients, introducing tensorial proportionality coefficients between the two.

If we consider in particular the momentum equation, the subgrid stress tensor τ_{ij} is assumed to be proportional to the strain rate tensor through a fourth order symmetric tensor as:

$$\tau_{ij} = -\overline{\rho}\Delta^2|\widetilde{\mathcal{S}}|\mathcal{B}_{ijrs}\widetilde{\mathcal{S}}_{rs}.\qquad(43)$$

The coefficient $\mathcal{B}_{ijrs}$ is dinamically computed following the procedure described in [1]. $\mathcal{B}_{ijrs}$ is rewritten as:

$$\mathcal{B}_{ijrs} = \sum_{\alpha,\beta=1}^{3}\mathcal{C}_{\alpha\beta}a_{i\alpha}a_{j\beta}a_{r\alpha}a_{s\beta},\qquad(44)$$

44

where a_{ij} is a rotation tensor and $\mathcal{C}_{\alpha\beta}$ is a second order symmetric tensor. As in [1] we set $a_{ij} = \delta_{ij}$ and the following expression is obtained for C_{ij}:

$$\mathcal{C}_{ij} = \frac{\mathcal{L}_{ij}}{\left(\widehat{\overline{\rho}\Delta^2|\widetilde{\mathcal{S}}|\widetilde{\mathcal{S}}_{ij}} - \widehat{\overline{\rho}}\widehat{\Delta}^2|\widecheck{\widetilde{\mathcal{S}}}|\widecheck{\widetilde{\mathcal{S}}}_{ij} \right)} \tag{45}$$

and

$$\tau_{ij} = -\overline{\rho}\Delta^2|\widetilde{\mathcal{S}}|\mathcal{C}_{ij}\widetilde{\mathcal{S}}_{ij}, \tag{46}$$

where no summation over the repeated indices is employed in the last formula.

As for the isotropic version of the dynamic model, the coefficients $\mathcal{C}_{ij}$ are averaged over each element and a clipping procedure is applied in order to ensure that the total dissipation is positive. Notice that, in the anisotropic version of the dynamic model, the deviatoric and isotropic parts of τ_{ij} are modeled together.

The dynamic procedure employed for the subgrid-scale stress in the momentum equation is applied also for the subgrid terms in the energy equation.

The subgrid heat flux is expressed as:

$$Q_i^{\text{sgs}} = -\overline{\rho}\Delta^2|\widetilde{\mathcal{S}}|\mathcal{B}_{ir}^Q\partial_r\widetilde{T}, \tag{47}$$

with $\mathcal{B}_{ir}^Q$ symmetric tensor. If $\mathcal{B}_{ir}^Q$ is diagonal, considering the reference frame defined by the tensor a, the following equation is obtained:

$$\mathcal{B}_{ir}^Q = \sum_{\alpha=1}^{3} \mathcal{C}_\alpha^Q a_{i\alpha} a_{r\alpha}. \tag{48}$$

Notice that the coefficients $\mathcal{C}_\alpha^Q$ can be computed via the dynamic procedure as in [1], obtaining:

$$\mathcal{C}_\alpha^Q = \frac{a_{i\alpha}\mathcal{L}_i^Q}{a_{r\alpha}\left(\widehat{\overline{\rho}\Delta^2|\widetilde{\mathcal{S}}|\partial_r\widetilde{T}} - \widehat{\overline{\rho}}\widehat{\Delta}^2|\widecheck{\widetilde{\mathcal{S}}}|\partial_r\widecheck{\widetilde{T}} \right)}. \tag{49}$$

The subgrid kinetic energy flux, given by equation (38), is modeled as:

$$\tau(u_i, u_k, u_k) = -\overline{\rho}\Delta^2|\widetilde{\mathcal{S}}|\mathcal{B}_{ir}^J\partial_r\left(\frac{1}{2}\widetilde{u}_k\widetilde{u}_k \right), \tag{50}$$

with:

$$\mathcal{B}_{ir}^J = \sum_{\alpha=1}^{3} \mathcal{C}_\alpha^J a_{i\alpha} a_{r\alpha}. \tag{51}$$

The coefficient $\mathcal{C}_\alpha^J$ is dinamically computed as:

$$\mathcal{C}_\alpha^J = \frac{a_{i\alpha}\mathcal{L}_i^J}{\mathcal{M}_\alpha}, \tag{52}$$

where

$$\mathcal{M}_\alpha = a_{r\alpha}\left(\overline{\rho}\Delta^2|\widetilde{\mathcal{S}}|\widehat{\partial_r\left(\frac{1}{2}\widetilde{u}_k\widetilde{u}_k\right)} - \widehat{\overline{\rho}}\widehat{\Delta}^2|\breve{\mathcal{S}}|\partial_r\left(\frac{1}{2}\breve{\widetilde{u}}_k\breve{\widetilde{u}}_k\right)\right). \tag{53}$$

Finally the subgrid turbulent diffusion flux takes the following form:

$$J_i^{\text{sgs}} = -\overline{\rho}\Delta^2|\widetilde{\mathcal{S}}|\mathcal{B}_{ir}^J\partial_r\left(\frac{1}{2}\widetilde{u}_k\widetilde{u}_k\right) + 2\widetilde{u}_k\tau_{ik} + \widetilde{u}_i\tau_{kk}. \tag{54}$$

B   Numerical method

The filtered Navier-Stokes equations are spatially discretized by the Discontinuous Galerkin finite elements method. The DG approach is analogous to that described in [22]. In particular the Local Discontinuous Galerkin (LDG) method is chosen for the approximation of the second order viscous terms (see [3], [4], [7], [11]). The Navier-Stokes equations (2) are rewritten in compact form and introducing an auxiliary variable $\mathcal{G}$, so that

$$
\begin{aligned}
\partial_t\mathbf{U} + \nabla\cdot\mathbf{F}^{\text{c}}(\mathbf{U}) &= \nabla\cdot\mathbf{F}^{\text{v}}(\mathbf{U},\mathcal{G}) \\
&- \nabla\cdot\mathbf{F}^{\text{sgs}}(\mathbf{U},\mathcal{G}) + \mathbf{S} \\
\mathcal{G} &- \nabla\boldsymbol{\varphi} = 0,
\end{aligned}
\tag{55}
$$

where $\mathbf{U} = [\overline{\rho}, \overline{\rho}\widetilde{\mathbf{u}}^T, \overline{\rho e}]^T$ are the prognostic variables, $\boldsymbol{\varphi} = [\widetilde{\mathbf{u}}^T, \widetilde{T}]^T$ are the variables whose gradients enter the viscous fluxes (3), as well as the turbulent ones and $\mathbf{S}$ represents the source terms. The fluxes in (55) are written in the following compact form:

$$\mathbf{F}^{\text{c}} = \left[\overline{\rho}\widetilde{\mathbf{u}}, \overline{\rho}\widetilde{\mathbf{u}}\otimes\widetilde{\mathbf{u}} + \overline{p}\mathcal{I}, \overline{\rho}\widetilde{h}\widetilde{\mathbf{u}}\right]^T,$$

$$\mathbf{F}^{\text{v}} = \left[0, \widetilde{\sigma}, \widetilde{\mathbf{u}}^T\widetilde{\sigma} - \widetilde{\mathbf{q}}\right]^T,$$

and

$$\mathbf{F}^{\text{sgs}} = \left[0, \tau, \frac{1}{(\gamma-1)Ma^2}\mathbf{Q}^{\text{sgs}} + \frac{1}{2}\left(\mathbf{J}^{\text{sgs}} - \tau_{kk}\widetilde{\mathbf{u}}\right)\right],$$

$$\mathbf{S} = [0, \overline{\rho}\mathbf{f}, \overline{\rho}\mathbf{f}\cdot\widetilde{\mathbf{u}}].$$

Here, τ, $\mathbf{Q}^{\text{sgs}}$ and $\mathbf{J}^{\text{sgs}}$ are given by (25), (27) and (28), respectively, for the Smagorinsky model, by (29), (36) and (42) for the isotropic

46

dynamic model and by (46), (47) and (54) for the anisotropic dynamic model.

To define the space discretization, a tessellation $\mathcal{T}_h$ of Ω into tetrahedral elements K is introduced such that $\Omega = \bigcup_{K \in \mathcal{T}_h} K$ and $K \cap K' = \emptyset$ and the finite element space is defined as:

$$\mathcal{V}_h = \left\{ v_h \in L^2(\Omega) : v_h|_K \in \mathbb{P}^p(K), \forall K \in \mathcal{T}_h \right\}, \qquad (56)$$

where p is a nonnegative integer and $\mathbb{P}^p(K)$ denotes the space of polynomial functions of total degree at most p on K. For each element, the outward unit normal on ∂K will be denoted by $\mathbf{n}_{\partial K}$. Given d the spatial dimension of the problem, the numerical solution is now defined as $(\mathbf{U}_h, \boldsymbol{\mathcal{G}}_h) \in \left((\mathcal{V}_h)^{(2+d)}, (\mathcal{V}_h)^{4 \times d} \right)$ such that, $\forall K \in \mathcal{T}_h, \forall v_h \in \mathcal{V}_h, \forall \mathbf{r}_h \in (\mathcal{V}_h)^d$,

$$\frac{d}{dt} \int_K \mathbf{U}_h v_h \, d\mathbf{x} - \int_K \mathbf{F}^{\mathrm{c}}(\mathbf{U}_h) \cdot \nabla v_h \, d\mathbf{x} \qquad (57a)$$

$$+ \int_K (\mathbf{F}^{\mathrm{v}} - \mathbf{F}^{\mathrm{sgs}})(\mathbf{U}_h, \boldsymbol{\mathcal{G}}_h) \cdot \nabla v_h \, d\mathbf{x} \qquad (57b)$$

$$+ \int_{\partial K} \mathbf{F}^{\mathrm{c},*}(\mathbf{U}_h, \mathbf{U}_h^+) \cdot \mathbf{n}_{\partial K} v_h \, d\sigma \qquad (57c)$$

$$- \int_{\partial K} (\mathbf{F}^{\mathrm{v}} - \mathbf{F}^{\mathrm{sgs}})(\boldsymbol{\varphi}^*, \boldsymbol{\mathcal{G}}^*) \cdot \mathbf{n}_{\partial K} v_h \, d\sigma = \int_K \mathbf{S} v_h \, d\mathbf{x},$$

$$\int_K \boldsymbol{\mathcal{G}}_h \cdot \mathbf{r}_h \, d\mathbf{x} + \int_K \boldsymbol{\varphi}_h \nabla \cdot \mathbf{r}_h \, d\mathbf{x} \qquad (57d)$$

$$- \int_{\partial K} \boldsymbol{\varphi}^* \mathbf{n}_{\partial K} \cdot \mathbf{r}_h \, d\sigma = 0,$$

where $\mathbf{U}_h = [\rho_h, \rho_h \mathbf{u}_h, \rho_h e_h]^T$ is the DG approximation of the solution into the element K, $\boldsymbol{\varphi}_h = [\mathbf{u}_h, T_h]^T$ are the quantities for which the gradient is computed, $\mathbf{F}^{\mathrm{c},*}$ is the numerical flux associated to the convective term, while $\boldsymbol{\varphi}^*$ and $\boldsymbol{\mathcal{G}}^*$ are the numerical fluxes for $\boldsymbol{\varphi}_h$ and $\boldsymbol{\mathcal{G}}_h$. The numerical fluxes are responsible for the coupling between elements. Notice that the symbols $\mathbf{U}_h$ and $\mathbf{U}_h^+$, when appearing as arguments of the numerical flux functions, assume the meaning described in the following. Consider the element K, the edge $e \in K$ and a point $\xi \in e$, we have:

$$\mathbf{U}_h = \mathbf{U}_h(\xi^{int(K)}) = \lim_{x \to \xi, x \in K} \mathbf{U}_h(x), \qquad (58a)$$

$$\mathbf{U}_h^+ = \mathbf{U}_h(\xi^{ext(K)}) = \lim_{x \to \xi, x \notin K} \mathbf{U}_h(x). \qquad (58b)$$

If only piecewise constant basis functions are considered, the weak formulation given by equations (57) defines implicitly the standard low order Finite Volume approaches. From this viewpoint, the Discontinuous Galerkin method can be seen as an extension to arbitrary order of accuracy of the Finite Volume method and, as a consequence, the well known exact and approximate Riemann solvers developed in the Finite Volume context can be successfully employed for the construction of the numerical flux $\mathbf{F}^{c,*}$ associated to the convective terms (see [36] for a comprehensive review of Riemann solvers). We have employed the exact Godunov Riemann solver implemented as in [23].

As already anticipated, the definition of the numerical flux for the viscous and subgrid terms is realized by means of the Local Discontinuous Galerkin (LDG) method. In particular we have extensively employed the method proposed in [4], obtaining:

$$\boldsymbol{\mathcal{G}}^* = \frac{1}{2} \left(\boldsymbol{\mathcal{G}}_h + \boldsymbol{\mathcal{G}}_h^+ \right),$$
$$\boldsymbol{\varphi}* = \frac{1}{2} \left(\boldsymbol{\varphi}_h + \boldsymbol{\varphi}_h^+ \right),$$

where the symbols have the same meaning as in equations (58).

Concerning the choice of the polynomial basis, on each element, the unknowns are expressed in terms of an orthogonal basis, yielding what is commonly called a modal DG formulation. All the integrals in equations (57) are evaluated using quadrature formulae from [14], which are exact for polynomial orders up to $2p$. This results in a diagonal mass matrix in the time derivative term of (57) and simplifies the computation of L^2 projections to be introduced in connection with the LES filters.

Notice that the fact that the quadrature formula employed for the numerical integration are exact for polynomial degrees up to $2p$ guarantees the exact integration of the mass matrix. However, the same quadrature rules are insufficient for the exact integration of the convective flux terms, which present more complex non-linearities. This may lead, expecially for high polynomial degrees ($p > 4$), to severe aliasing errors which tipically cause instabilities and crashing of the computation due to the generation of strong unphysical oscillations, which are the cause of the violation of the constitutive laws [5]. Notice that, in [5], it is pointed out that, also in the case of low order polynomial degrees ($p \leq 2$) and mid range polynomial degrees, such as $p = 3$, for which stability is not a problem due to the presence of sufficient numerical dissipation, which counteracts the

aliasing effect, the aliasing terms may negatively influence the solution: the interaction between discretization, aliasing and subgrid model dissipation gives indeed rise to inaccurate results.

A possible solution to the aliasing issue is the so called polynomial de-aliasing, first introduced in [28]: the numerical quadrature precision is increased such that the convective flux integrals can be evaluated exactly with respect to the machine precision. Notice that, as discussed in [5], the introduction of a de-aliasing procedure is important because in this way the physically based turbulence models can better carry out their role of modeling the missing subgrid-scale physics and are not relegated to countering the numerical instabilities arising from aliasing errors.

In the following the filter operators $\bar{\cdot}$ and $\widehat{\cdot}$, introduced in section 2, will be explicitly defined in the context of the DG finite elements method. In particular, following a VMS approach, filter operators are identified with an L^2 projection, as suggested e.g. in [12], [13], [41] and [1]. Given a subspace $\mathcal{V} \subset L^2(\Omega)$, let $\Pi_{\mathcal{V}} : L^2(\Omega) \to \mathcal{V}$ be the associated projector defined by

$$\int_{\Omega} \Pi_{\mathcal{V}} u \, v \, d\mathbf{x} = \int_{\Omega} u \, v \, d\mathbf{x}, \qquad \forall u, v \in \mathcal{V},$$

where the integrals are evaluated with the same quadrature rule used in (57). For $v \in L^2(\Omega)$, the filter $\bar{\cdot}$ is now defined by

$$\overline{v} = \Pi_{\mathcal{V}_h} v. \tag{60}$$

Notice that the application of this filter is built in the discretization process and equivalent to it. Therefore, once the discretization of equations (55) has been performed, only $\bar{\cdot}$ filtered quantities are computed by the model. To define the test filter, we introduce

$$\widehat{\mathcal{V}}_h = \left\{ v_h \in L^2(\Omega) : v_h|_K \in \mathbb{P}^{\widehat{p}}(K), \forall K \in \mathcal{T}_h \right\}, \tag{61}$$

where $0 \leq \widehat{p} < p$, and we let, for $v \in L^2(\Omega)$,

$$\widehat{v} = \Pi_{\widehat{\mathcal{V}}_h} v. \tag{62}$$

By our previous identification of the $\bar{\cdot}$ filter and the discretization, the quantities $\overline{\rho}$, $\overline{\rho \widetilde{\mathbf{u}}}$ and $\overline{\rho \widetilde{e}}$ can be identified with ρ_h, $\rho_h \mathbf{u}_h$ and $\rho_h e_h$, respectively. Therefore they belong to $\mathcal{V}_h$, for which an orthogonal basis is employed by the numerical method. As a result, the computation of $\widehat{\rho_h}$, $\widehat{\rho_h \mathbf{u}_h}$ and $\widehat{\rho_h e_h}$ is straightforward and reduces to zeroing the last coefficients in the local expansion. Assuming that the analytic solution is defined in some infinite dimensional subspace

of L^2, heuristically, $\mathcal{V}_h \subset L^2$ is associated to the scales which are represented by the model, while $\widehat{\mathcal{V}}_h \subset \mathcal{V}_h \subset L^2$ is associated to the spatial scales well resolved by the numerical approximation.

The spatial scales Δ and $\widehat{\Delta}$ associated with the two filters (60) and (62) can be computed as:

$$\Delta = \left(\frac{\Delta_x \Delta_y \Delta_z}{N_p} \right)^{1/3}, \quad \widehat{\Delta} = \left(\frac{\Delta_x \Delta_y \Delta_z}{N_{\widehat{p}}} \right)^{1/3}, \qquad (63)$$

where N_p and $N_{\widehat{p}}$ are the number of degrees of freedom per element associated to the polynomial degrees p and $\widehat{p}$, respectively and Δ_x, Δ_y and Δ_z are equivalent grid spacings computed as in equations (13). The filter scales are, as a consequence, piecewise polynomial functions in space.

Acknowledgements

References

[1] A. Abbà, L. Bonaventura, M. Nini, and M. Restelli. Dynamic models for Large Eddy Simulation of compressible flows with a high order DG method. *Computers & Fluids*, 122:209–222, 2015.

[2] A. Abbà, C. Cercignani, and L. Valdettaro. Analysis of Subgrid Scale Models. *Computer and Mathematics with Applications*, 46:521–535, 2003.

[3] D. N. Arnold, F. Brezzi, B. Cockburn, and L.D. Marini. Unified analysis of Discontinuous Galerkin methods for elliptic problems. *SIAM Journal of Numerical Analysis*, 39:1749–1779, 2002.

[4] F. Bassi and S. Rebay. High Order Accurate Discontinuous Finite Element Method for the Numerical Solution of the Compressible Navier-Stokes Equations. *Journal of Computational Physics*, 131:267–279, 1997.

[5] A. Beck, D.G. Flad, C. Tonhäuser, G. Gassner, and C.D. Munz. On the influence of polynomial de-aliasing on subgrid scale models. *Flow Turbulence Combust.*, 97:475–511, 2016.

[6] V. K. Birman, J.E. Martin, and E. Meiburg. The non-Boussinesq Lock-exchange problem. Part 2. High-resolution simulations. *Journal of Fluid Mechanics*, 537:125–144, 2005.

[7] P. Castillo, B. Cockburn, I. Perugia, and D. Schötzau. An a priori analysis of the Local Discontinuous Galerkin method for elliptic problems. *SIAM Journal of Numerical Analysis*, 38:1676–1706, 2000.

[8] C.Bassi. *Large Eddy Simulation of compressible variable density flows with a high-order DG-LES model.* PhD thesis, Politecnico di Milano, 2018.

[9] C.Bassi, A. Abbà, L. Bonaventura, and L. Valdettaro. Large Eddy Simulation of gravity currents with a high-order DG method. *Communications in Applied and Industrial Mathematics*, 8:128–148, 2017.

[10] C.Bassi, A. Abbà, L. Bonaventura, and L. Valdettaro. A priori tests of a novel LES approach to compressible variable density turbulence. Technical Report 20/2018, MOX, Politecnico di Milano, 2018.

[11] B. Cockburn and C.W. Shu. The Local Discontinuous Galerkin Method for Time-Dependent Convection Diffusion Systems. *SIAM Journal of Numerical Analysis*, 35:2440–2463, 1998.

[12] S. S. Collis. Discontinuous Galerkin methods for turbulence simulation. In *Proceedings of the 2002 Center for Turbulence Research Summer Program*, pages 155–167, 2002.

[13] S. S. Collis and Y. Chang. The DG/VMS method for unified turbulence simulation. *AIAA paper*, 3124:24–27, 2002.

[14] R. Cools. An Encyclopaedia of Cubature Formulas. *Journal of Complexity*, 19:445–453, 2003.

[15] M. Dumbser and V. Casulli. A conservative, weakly nonlinear semi-implicit finite volume scheme for the compressible Navier-Stokes equations with general equation of state. *Applied Mathematics and Computation*, 272:479–497, 2016.

[16] E. Garnier, N. Adams, and P. Sagaut. *Large Eddy Simulation for Compressible Flows.* Springer Verlag, 2009.

[17] M. Germano. Turbulence: the filtering approach. *Journal of Fluid Mechanics*, 238:325–336, 1992.

[18] M. Germano, A. Abbà, R. Arina, and L. Bonaventura. On the extension of the eddy viscosity model to compressible flows. *Physics of Fluids*, 2014.

[19] M. Germano, U. Piomelli, P. Moin, and W.H. Cabot. A Dynamic Subgrid-Scale Eddy Viscosity Model. *Physics of Fluids*, 3(7):1760–1765, 1991.

[20] A.E. Gill. *Atmosphere-Ocean Dynamics.* Academic Press, 1982.

[21] F.X. Giraldo, J.F. Kelly, and E.M. Constantinescu. Implicit-Explicit formulations of a three-dimensional Nonhydrostatic Unified Model of the Atmosphere (NUMA). *SIAM, J. Sci. Comput.*, 35:B1162–B1194, 2013.

[22] F.X. Giraldo and M. Restelli. A study of spectral element and discontinuous galerkin methods for the navier-stokes equations in nonhydrostatic mesoscale atmospheric modelling: equation sets and test cases. *Journal of Computational Physics*, 227:3849–3877, 2008.

[23] J.J. Gottlieb and C.P.T. Groth. Assessment of Riemann Solvers for Unsteady One-Dimensional Inviscid Flows of Perfect Gases. *Journal of Computational Physics*, 78:437–458, 1988.

[24] C. Härtel, E. Meiburg, and F. Necker. Analysis and direct numerical simulation of the flow at a gravity-current head. Part 1. Flow topology and front speed for slip and no-slip boundaries. *Journal of Fluid Mechanics*, 418:189–212, 2000.

[25] T.J.R Hughes, L. Mazzei, and A.A. Oberai. Large Eddy Simulation of turbulent channel flows by the variational multiscale method. *Physics of Fluids*, 13:1784–1799, 2001.

[26] J.C.R. Hunt, A. Wray, and P. Moin. Eddies, stream, and convergence zones in turbulent flows. Technical Report CTR-S88, Center for Turbulence Research, 1988.

[27] V. John and A. Kindl. Numerical studies of finite element Variational Multiscale Methods for turbulent flow simulations. *Computer Methods in Applied Mechanics and Engineering*, 199:841–852, 2010.

[28] R.M. Kirby and G.E. Karniadakis. De-aliasing on non-uniform grids: algorithms and applications. *Journal of Computational Physics*, 191:249–264, 2003.

[29] T.M. Özgökmen, T. Iliescu, and P.F. Fischer. Large Eddy Simulation of stratified mixing in a three-dimensional Lock-exchange system. *Ocean Modelling*, 26:134–155, 2009.

[30] T.M. Özgökmen, T. Iliescu, P.F. Fischer, A. Srinivasan, and J. Duan. Large Eddy Simulation of stratified mixing in two-dimensional dam-break problem in a rectangular enclosed domain. *Ocean Modelling*, 16:106–140, 2007.

[31] U. Piomelli, W.H. Cabot, P. Moin, and S. Lee. Subgrid -scale backscatter in turbulent and transitional flows. *Physics of Fluids*, 3:1766–1771, 1991.

[32] P. Sagaut. *Large Eddy Simulation for Incompressible Flows: An Introduction.* Springer Verlag, 2006.

[33] J.E. Simpson. *Gravity currents in the environment and in the laboratory.* Cambridge University Press, 1997.

[34] J. Smagorinsky, S. Manabe, and J. Leith Holloway. Numerical results from a nine-level general circulation model of the athmosphere. *Monthly weather Review*, 93:727–768, 1965.

[35] R.J. Spiteri and S.J. Ruuth. A new class of optimal high-order Strong Stability Preserving time discretization methods. *SIAM Journal of Numerical Analysis*, 40:469–491, 2002.

[36] E.F. Toro. *Riemann Solvers and Numerical Methods for Fluid Dynamics, a Practical Introduction.* Springer, 2009.

[37] Y. Tseng and J.H. Ferziger. Mixing and available potential energy in stratified flows. *Physics of Fluids*, 13:1281–1293, 2001.

[38] M. Tugnoli, A.Abbà, L. Bonaventura, and M. Restelli. A locally p-adaptive approach for Large Eddy Simulation of compressible flows in a DG framework. *Journal of Computational Physics*, 349:33–58, 2017.

[39] G. Tumolo and L. Bonaventura. A semi-implicit, semi-Lagrangian, DG framework for adaptive numerical weather prediction. *Quarterly Journal of the Royal Meteorological Society*, 141:2582–2601, 2015.

[40] G. Tumolo, L. Bonaventura, and M. Restelli. A semi-implicit, semi-Lagrangian, p-adaptive discontinuous Galerkin method for the shallow water equations. *Journal of Computational Physics*, 231:46–67, 2013.

[41] F. Van der Bos, J.J.W. Van der Vegt, and B.J. Geurts. A multi-scale formulation for compressible turbulent flows suitable for

general variational discretization techniques. *Computer Methods in Applied Mechanics and Engineering*, 196:2863–2875, 2007.

[42] K.B. Winters, P.N. Lombard, J.J. Riley, and E.A. D'Asaro. Available potential energy and mixing in density-stratified fluids. *Journal of Fluid Mechanics*, 289:115–128, 1995.

MOX Technical Reports, last issues

Dipartimento di Matematica
Politecnico di Milano, Via Bonardi 9 - 20133 Milano (Italy)

22/2018 Pegolotti, L.; Dede', L.; Quarteroni, A.
Isogeometric Analysis of the electrophysiology in the human heart: numerical simulation of the bidomain equations on the atria

23/2018 Benacchio, T.;Bonaventura,L.
A seamless extension of DG methods for hyperbolic problems to unbounded domains

21/2018 Gervasio, P.; Dede', L.; Chanon, O.; Quarteroni, A.
Comparing Isogeometric Analysis and Spectral Element Methods: accuracy and spectral properties

20/2018 Bassi, C. ; Abbà, A.; Bonaventura L.; Valdettaro, L.
A priori tests of a novel LES approach to compressible variable density turbulence

19/2018 Menghini, F.; Dede', L.; Quarteroni, A.
Variational Multiscale LES modeling of blood flow in an idealized left human heart

18/2018 Antonietti, P.F.; Bonaldi, F.; Mazzieri, I.
A high-order discontinuous Galerkin approach to the elasto-acoustic problem

16/2018 Calissano, A.; Vantini, S.; Arnaboldi, M.
An elephant in the room: Twitter samplingmethodology.

15/2018 Simona, A.; Bonaventura, L.; Pugnat, T.; Dalena, B.
High order time integrators for the simulation of charged particle motion in magnetic quadrupoles

14/2018 Cuffaro, M.; Miglio, E.; Penati, M.;Viganò, M.
Mantle upwelling driven by asymmetric sea-floor spreading at northern Mid–Atlantic ridge

17/2018 Agosti, A.; Giverso, C.; Faggiano, E.;Stamm,A.; Ciarletta, P.
A personalized mathematical tool for neuro-oncology: a clinical case study